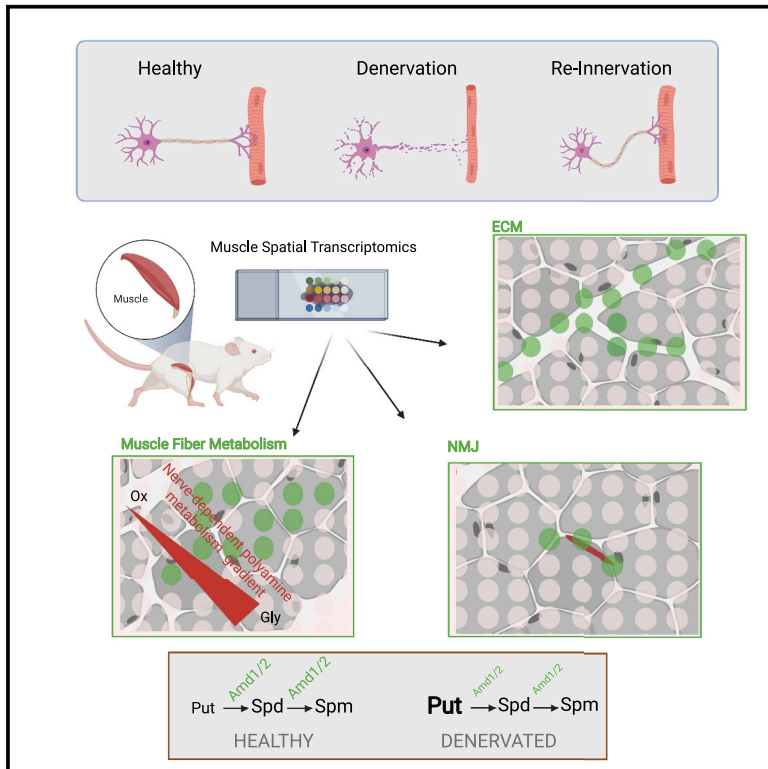# Spatially resolved transcriptomics reveals innervation-responsive functional clusters in skeletal muscle

Graphical abstract

Authors

Chiara D'Ercole, Paolo D'Angelo, Veronica Ruggieri, ..., Claudio Sette, Lorenzo Giordani, Luca Madaro

Correspondence

lorenzo.giordani@sorbonne-universite.fr (L.G.),
luca.madaro@uniroma1.it (L.M.)

In brief

Using spatially resolved transcriptomics, D'Ercole et al. have analyzed the different morphofunctional domains in muscle and their response to reversible nerve damage, highlighting the polyamine pathway as a potential contributor to the atrophic response.

Highlights

- Characterization of functional cluster in adult muscle using spatial transcriptomics

- Identification of differentially activated pathway during denervation

- Polyamine pathway is spatially restricted and innervation responsive

CellPress

Resource

Spatially resolved transcriptomics reveals innervation-responsive functional clusters in skeletal muscle

Chiara D'Ercole,[1,2] Paolo D'Angelo,[1,2] Veronica Ruggieri,[1,2] Daisy Proietti,[3] Laura Virtanen,[4] Cristina Parisi,[1,2] Carles Sanchez Riera,[1] Alessandra Renzini,[1] Alberto Macone,[5] Marta Marzullo,[6] Laura Ciapponi,[7] Davide Bonvissuto,[8] Claudio Sette,[8,9] Lorenzo Giordani,[4,*] and Luca Madaro[1,2,10,*]

[1]Department of Anatomical, Histological, Forensic Sciences and Orthopedics, Sapienza University of Rome, 00161 Rome, Italy
[2]Laboratory Affiliated to Istituto Pasteur Italia-Fondazione Cenci Bolognetti, 00161 Rome, Italy
[3]Cell Therapy for Myopathies Unit, Division of Neurosciences, San Raffaele Hospital, 20132 Milano, Italy
[4]Sorbonne Université, INSERM UMRS 974, Association Institut de Myologie, Centre de Recherche en Myologie, 75013 Paris, France
[5]Department Biochemical Sciences, Sapienza University of Rome, 00185 Rome, Italy
[6]IBPM CNR c/o Department of Biology and Biotechnology, Sapienza University of Rome, 00185 Rome, Italy
[7]Department of Biology and Biotechnologies, Sapienza University of Rome, 00185 Rome, Italy
[8]Department of Neuroscience, Section of Human Anatomy, Catholic University of the Sacred Heart, 00168 Rome, Italy
[9]GSTeP Organoids Research Core Facility, Fondazione Policlinico A. Gemelli, 00168 Rome, Italy
[10]Lead contact
*Correspondence: lorenzo.giordani@sorbonne-universite.fr (L.G.), luca.madaro@uniroma1.it (L.M.)
https://doi.org/10.1016/j.celrep.2022.111861

SUMMARY

Striated muscle is a highly organized structure composed of well-defined anatomical domains with integrated but distinct assignments. So far, the lack of a direct correlation between tissue architecture and gene expression has limited our understanding of how each unit responds to physio-pathologic contexts. Here, we show how the combined use of spatially resolved transcriptomics and immunofluorescence can bridge this gap by enabling the unbiased identification of such domains and the characterization of their response to external perturbations. Using a spatiotemporal analysis, we follow changes in the transcriptome of specific domains in muscle in a model of denervation. Furthermore, our approach enables us to identify the spatial distribution and nerve dependence of atrophic signaling pathway and polyamine metabolism to glycolytic fibers. Indeed, we demonstrate that perturbations of polyamine pathway can affect muscle function. Our dataset serves as a resource for future studies of the mechanisms underlying skeletal muscle homeostasis and innervation.

INTRODUCTION

Skeletal muscle is a complex organ in which several mononucleated cell populations organize within specific anatomic compartments. These domains—nerves, connective, and vasculature—act together in coordination with muscle fibers to ensure the seamless execution of each contraction. In response to acute injury, specific resident muscle populations activate and contribute to regeneration by regulating muscle stem cell activity or cooperating with immune cells recruited from the circulatory system (neutrophils, macrophages).[1] However, muscle regeneration is not limited to myofiber repair; in order for the muscle to be functional, all the different compartments need to be repaired. Indeed, voluntary contraction can only be restored through the establishment of new neuromuscular junctions (NMJs) on the newly formed myofibers.[2] Innervation not only enables voluntary muscle control but also contributes to the maintenance of tissue homeostasis by regulating the balance between anabolic and catabolic responses.[3]

Recently, due to the advent of single-cell RNA sequencing (scRNA-seq) and single-nucleus RNA sequencing (snRNA-seq), the heterogeneity of muscle cellular populations and their relative role under physiological and pathological conditions such as injury, denervation, or genetic disorders have begun to be methodically surveyed.[4–16] However, these approaches have several intrinsic limitations that hinder our ability to fully understand skeletal muscle pathophysiology. In particular, most of skeletal muscle mass is composed of long, polynucleated fibers, which, due to the necessary dissociation step, are incompatible with the analysis of cytoplasmic RNAs.

Moreover, functional anatomical domains such as NMJs, tendon-to-muscle connections, vessels, and connective tissue can have different interactions depending on their relative proximity and locations; unfortunately, upon processing for single-cell analysis, the tissue architecture is disrupted, and this higher-order information is lost. As a consequence of this, the complexity of muscle tissue in pathophysiological conditions, in terms of both cellular heterogeneity and spatial

A

B

C
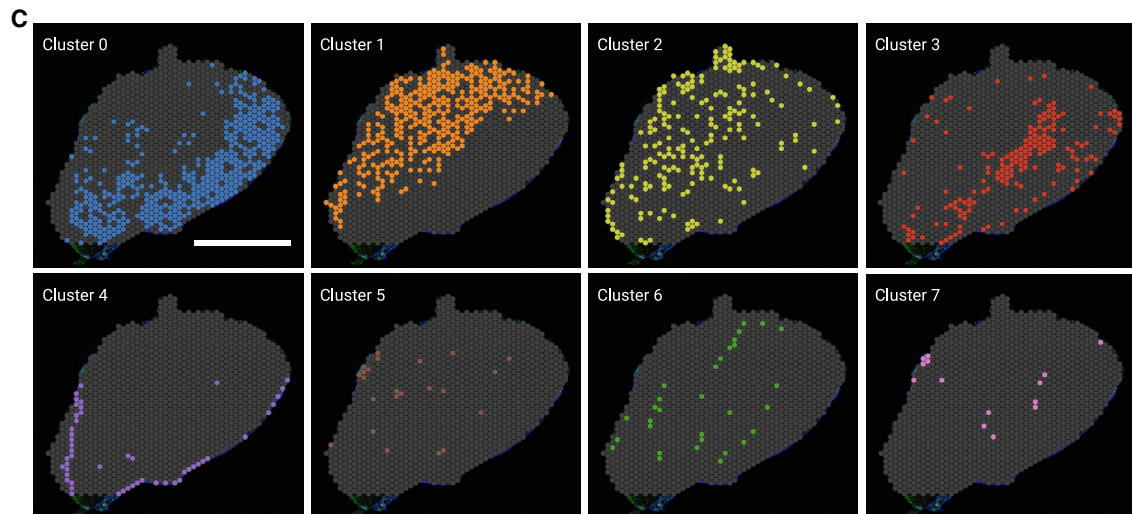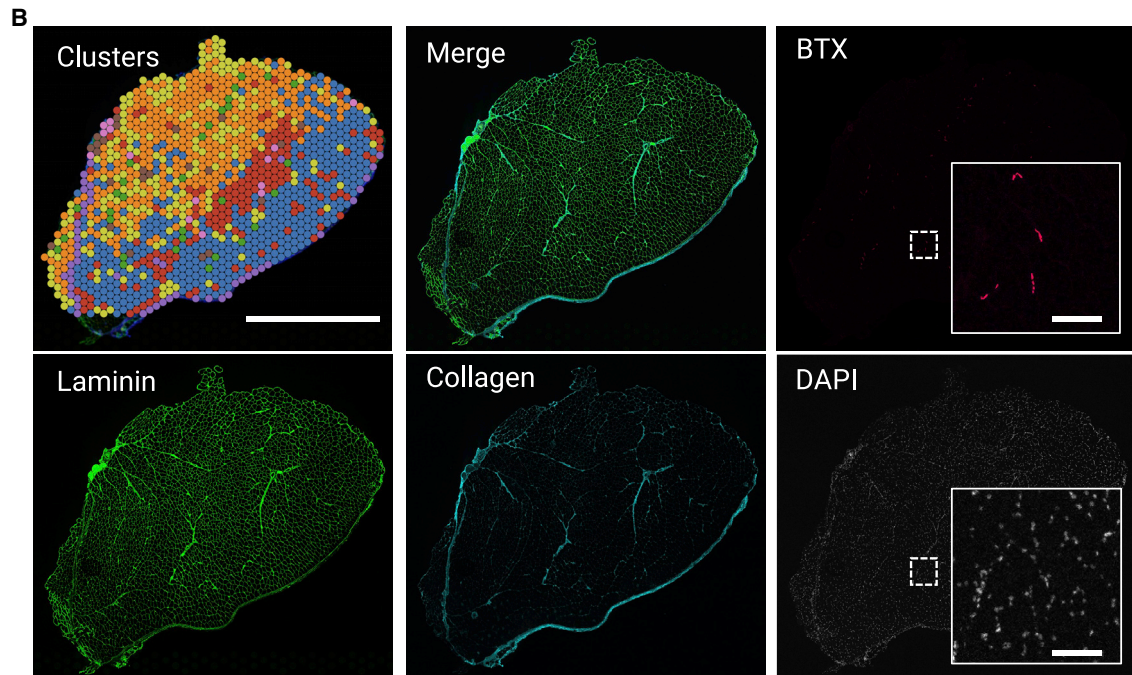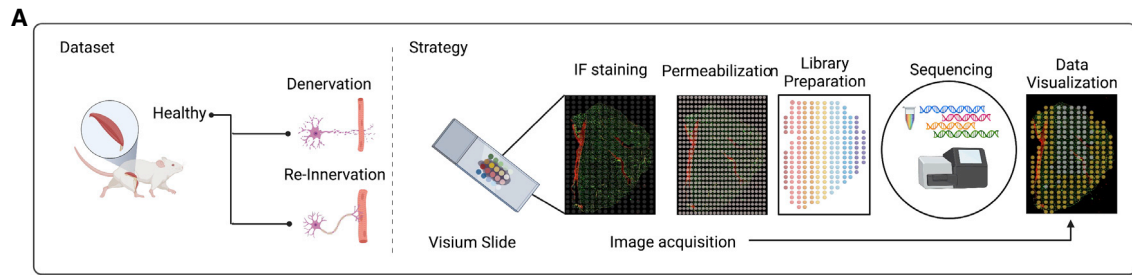
(legend on next page)

relocalization, has not yet been fully described. Despite recent advances,[10,11,13] our understanding of how traumatic events such as nerve injury differentially influence the specific anatomical domains and the various cellular identities remains incomplete. In this context, spatial transcriptomics (ST) could contribute to a revolution in the field of muscle "omics" as a fusion of recent sequencing technologies and classical histology.[17–20]

Thus, by using ST, we aimed to characterize the discrete molecular signature of the different anatomical domains in skeletal muscle and investigate their relative role in the well-characterized model of nerve crush injury. Coupling ST with immunofluorescence, we first unbiasedly identified functional anatomical clusters in healthy muscle. Then, probing the muscle at different timepoints, we evaluated their specific transcriptomic alterations during reinnervation. Capitalizing on ST, we identified multiple key enzymes of the polyamine pathway as innervation dependent and restricted to glycolytic fibers. Lastly, we showed how perturbations of such pathway can impact muscle function. Our data define the transcriptional profile of the different anatomical compartments in skeletal muscle and set the basis for the understanding of differential fiber sensitivity to atrophy and nerve-dependent gene expression. The dataset can be fully accessed via the SpatialMuscle web resource (https://spatialmuscle.shinyapps.io/spatialmuscle/).

RESULTS

Spatial transcriptome analysis identifies eight different clusters in muscle tissue

To establish a transcriptional reference of the different skeletal muscle anatomical domains and investigate their response to denervation, we took advantage of the Visium Spatial Gene Expression platform (10x Genomics). Mouse limb tibialis anterior (TA, tibial muscle) and associated extensor digitorum longus (EDL) were harvested before and after reversible nerve injury, at different timepoints (3 and 30 days after sciatic nerve compression; experimental workflow is shown in Figure 1A). Muscle cryosections were then placed on Visium slide capture areas and stained. Each area contains ~5,000 RNA capture spots characterized by a specific spatial barcode that ensures that transcripts can be mapped to their original histological location. To highlight the different anatomical features of the muscle, we used anti-laminin and anti-collagen-1 antibodies, bungarotoxin (BTX), and DAPI. This strategy enabled us to visualize fiber boundaries, extracellular matrix scaffolds, NMJs, and cellular nuclei, respectively (Figures 1B, S1A, and S1B). After imaging, tissue was permeabilized, and polyadenylated RNA was captured on the underlying spots. Following manufacturer protocols, we performed reverse transcription, second strand synthesis, and amplification. After library preparation and sequencing,

reads were processed and spatially resolved using Space Ranger software. The different datasets were then analyzed separately and integrated using Seurat 4[21]. Lastly, data were overlaid onto the acquired image of the tissue sections (Figures 1B, S1A, and S1B). Overall, we identified 14,417 features across 2,987 unique capture spots. Unsupervised clustering identified eight clusters with consistent transcript abundance distribution (Figure S1C). Tissue projection showed clear spatial segregation for four out of the eight clusters (clusters 0, 1, 3, 4) (Figures 1C, S1D, and S1E). This specific spatial arrangement readily suggested that these clusters could represent the major metabolic domains and general areas of the muscle such as different types of fibers or specific components of the matrix scaffold. Conversely, clusters 2, 5, 6, and 7 showed a sparse distribution more in line with small functional elements dispersed within the tissue such as NMJs, vessels, or nerves. Based on this initial observation, we therefore set out to determine the identity of each of these specific cluster based on their gene expression profile (Table S1) and their overlap with pre-annotated anatomical structures in the uninjured muscle.

Spatial transcriptomic clustering reveals functional and structural organization of muscle tissue
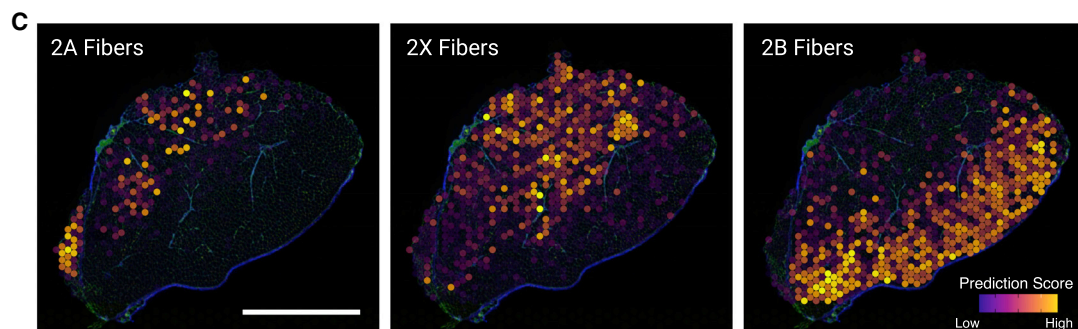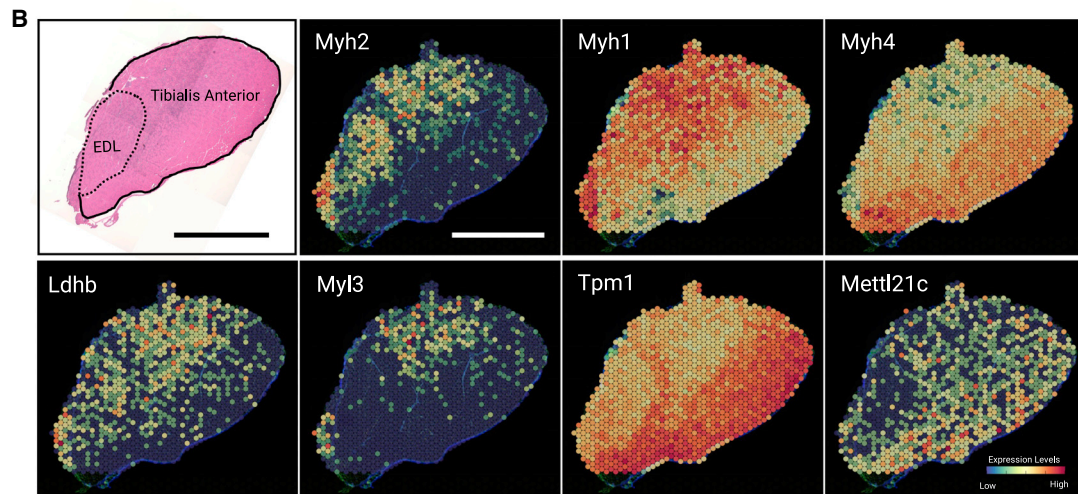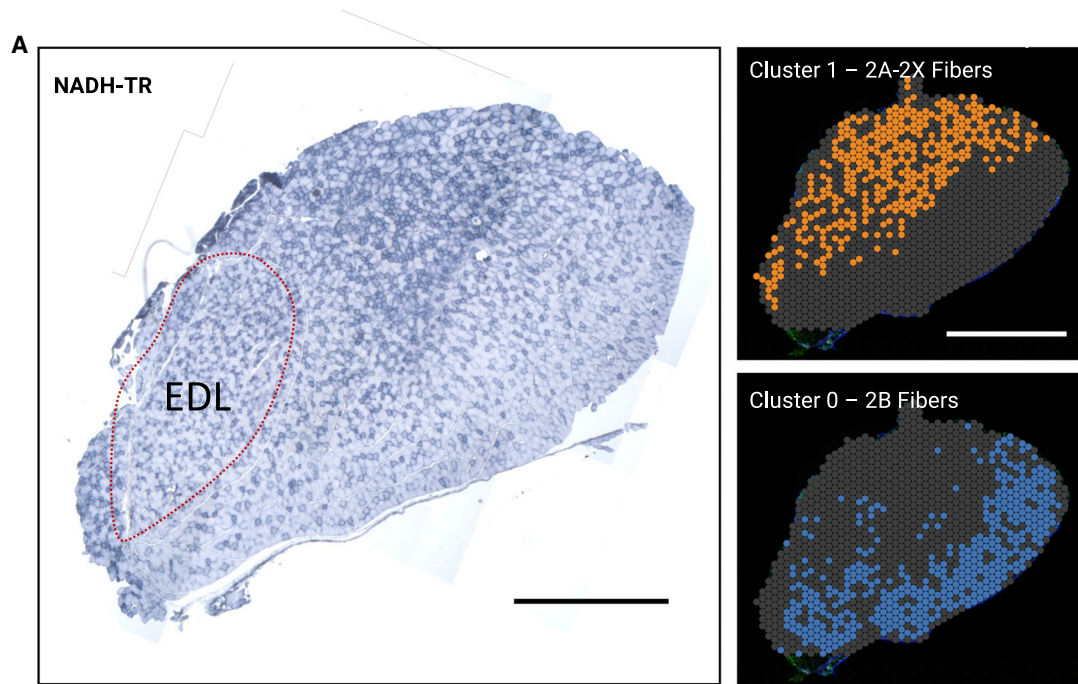
We initially correlated the distribution of genes in unbiased predicted clusters with functionally characterized muscle areas. As shown by the NADH-TR (nicotinamide adenine dinucleotide tetrazolium reductase) staining—used to identify areas with high oxidative activity—TA muscle is characterized by a glycolytic cortex, in which muscle fibers are predominantly lightly stained, and by a darker oxidative core (Figure 2A). Indeed, staining intensity directly correlates with the number of mitochondria within a muscle fiber and reveals the characteristic pattern of finer fiber types. Based on their metabolic properties and the specific myosin subsets, expressed muscle fibers can be divided in slow twitching (type 1) and fast twitching (type 2). TA is primarily composed of type 2 fibers, which can be further subdivided into three main categories (2A oxidative, 2X, and 2B glycolytic). Interestingly, whereas cluster 1 was associated with the deeper oxidative core of the muscle normally characterized by the presence of 2A fibers, cluster 0 overlapped with the glycolytic cortex of the tibialis containing mostly 2B fibers (Figure 2A). Indeed, Gene Ontology (GO) analyses of cluster 1 genes revealed the enrichment of terms associated with mitochondrial structure and respiration (Figure S2A) and as expected, cells in the two clusters expressed canonical markers of specific fiber types. For example, myosin heavy chain 2 (Myh2, characteristic of 2A fibers), lactate dehydrogenase B (Ldhb) post-glycolytic enzyme, and slow fiber markers such as Myl3 were spatially restricted to cluster 1, while the fast twitch glycolytic myosin isoform 4 (Myh4) and the associated fast isoform of tropomyosin (Tpm1) primarily co-segregated into cluster 0 (Figure 2B).

Figure 1. Spatially resolved transcriptomics highlights discrete functional anatomical units

(A) Diagram illustrating the experimental workflow for spatial transcriptomics (ST) analysis using 10x Visium slide.

(B) WT mouse hindlimb cryosection (TA and EDL) used for ST analysis. Visium array spots are color-coded based on cluster assignment of the integrated dataset (top left). Immunofluorescence staining for bungarotoxin (BTX) (top right), laminin (bottom left), collagen-1 (bottom center), and DAPI (bottom right) (scale bar, 2 mm; inset scale bar, 100 μm).

(C) Spatial distribution of each cluster (scale bar, 2 mm).

A NADH-TR

Cluster 1 – 2A-2X Fibers

Cluster 0 – 2B Fibers

B Tibialis Anterior / EDL

Myh2 | Myh1 | Myh4

Ldhb | Myl3 | Tpm1 | Mettl21c

Expression Levels
Low — High

C 2A Fibers | 2X Fibers | 2B Fibers

Prediction Score
Low — High

(legend on next page)

However, the distribution of other genes known to be involved in the development of glycolytic fibers (e.g., *Sox6*, *Fnip1*, *Tbx15*, and *Smarcd3* [*Baf60c*])[21–24] is not confined to cluster 0, probably because of the high level of expression of these genes in structures with different origins (e.g., vessels, extracellular matrix, nerves, etc.) or because of their different roles in adult tissue (Figures S2B and 2C).

Notably, the ST profile confirmed that expression of the *Mettl21c* gene is confined to the tibialis and almost absent from the EDL muscle (Figure 2B), as previously reported.[25] In addition, in cluster1, we also detected the expression of myosin heavy chain 1 (*Myh1*), a hallmark of 2X fibers (Figure 2B). We speculated that, given their phenotype, intermediate between 2A and 2B in terms of contraction velocities and mitochondrial activity,[26] these fibers could also be present in cluster1.

To test this hypothesis and further validate our annotations, we integrated our ST data with a previously published single-nucleus RNA sequencing (WT dataset from Chemello and colleagues[4]), and we spatially mapped cell type predictions for the different fiber types (see STAR Methods). Data intersection confirmed that fiber-type metabolism was correctly predicted based on the spatial distribution of the myosin types identified in each cluster (Figure 2C). While the glycolytic portion, overlapping with cluster 0, was predicted to contain type 2B fibers (fast glycolytic), the portion overlapping with cluster 1 consisted of type 2A fibers (fast oxidative) and type 2X fibers, which are less glycolytic than type 2B fibers (Figure 2C). This observation was also confirmed by immunofluorescent staining of fiber types 2A and 2B from a serial section (Figure S2D).

Next, we analyzed the molecular signature of the other two clusters that presented a clear spatial distribution, cluster 3 and cluster 4. Upon GO analysis, both clusters 3 and 4 displayed an enrichment in extracellular matrix components (Figure S3A). However, while cluster 3 overlapped considerably with the muscular matrix scaffold, cluster 4 clearly identified the epimysium surrounding the muscle (Figures 3A and S3B). Almost perfect overlap was obtained between the localization of cluster 4 and the localization of collagen type 1 surrounding the muscle (validated by immunofluorescence and Sirius red staining; Figure 3A, inset). As expected, the genes enriched in this cluster are extracellular matrix components such as collagen subunits (*Col12a1* and *Col1a1*) and matrix-associated molecules (*Fmod* and *Timp2*) (Figure 3B).

Given the complexity of muscle tissue, we wondered whether ST analysis might not only reveal more abundant clusters related to muscle fibers but also identify more restricted morphofunctional zones specific to this tissue. We therefore analyzed the gene expression signature of the sparse clusters (cluster 2, cluster 5, cluster 6, cluster 7) and their relative spatial proximity to known morphological structures. Upon visual inspection, cluster 2 did not present a recognizable distribution pattern nor overlap with clearly detectable anatomical compartments. Furthermore, we could not detect a strong gene expression signature for the cluster. However, it must be considered that each spot contains data from an ensemble of different cell types, and it is possible that transition areas where such a mix is more diverse could be clustered together. This could explain the weak gene signature and the associated generic GO terms (muscle contraction and muscle system process; Figure S3C).

Additionally, it is worth mentioning that the expressed genes identified included *Alas2* and different hemoglobin transcripts, suggesting specific erythroid enrichment (Table S1). Thus, at least some of these regions could contain small blood vessels.

Cluster 6 spots, on the other hand, nicely colocalized with acetylcholine receptor across muscle sections (stained with Alexa 594-conjugated BTX; Figure 3C). In line with the spatial pattern, GO analysis of genes enriched in cluster 6 contained terms associated with NMJs and synapses (Figure S3D). As further validation, NMJ location prediction based on Chemello and colleagues[4] snRNA-seq integration overlapped with cluster 6 spots (Figure 3C). Lastly, representative genes of this cluster encode acetylcholine receptor subunits (*Chrne*, *Chrnd*, *Chrna1*) or transcription factors known to be expressed in subsynaptic nuclei (*Etv5*)[9] (Figure 3D).

Interestingly enough, clusters 5 and 7 also correlated with histological structures, associating respectively with nerves and large vessels. Indeed, cluster 5 was enriched in glial- (*Plp1)* and myelin- (*Pmp22*, *Mpz*, and *Mbp*) associated factors, while cluster 7 expressed endothelial- or smooth muscle-associated genes (*CD31-Pecam1*, *Vwf*, *Myh11*, and *Acta2*) (Figures 4A and 4B).
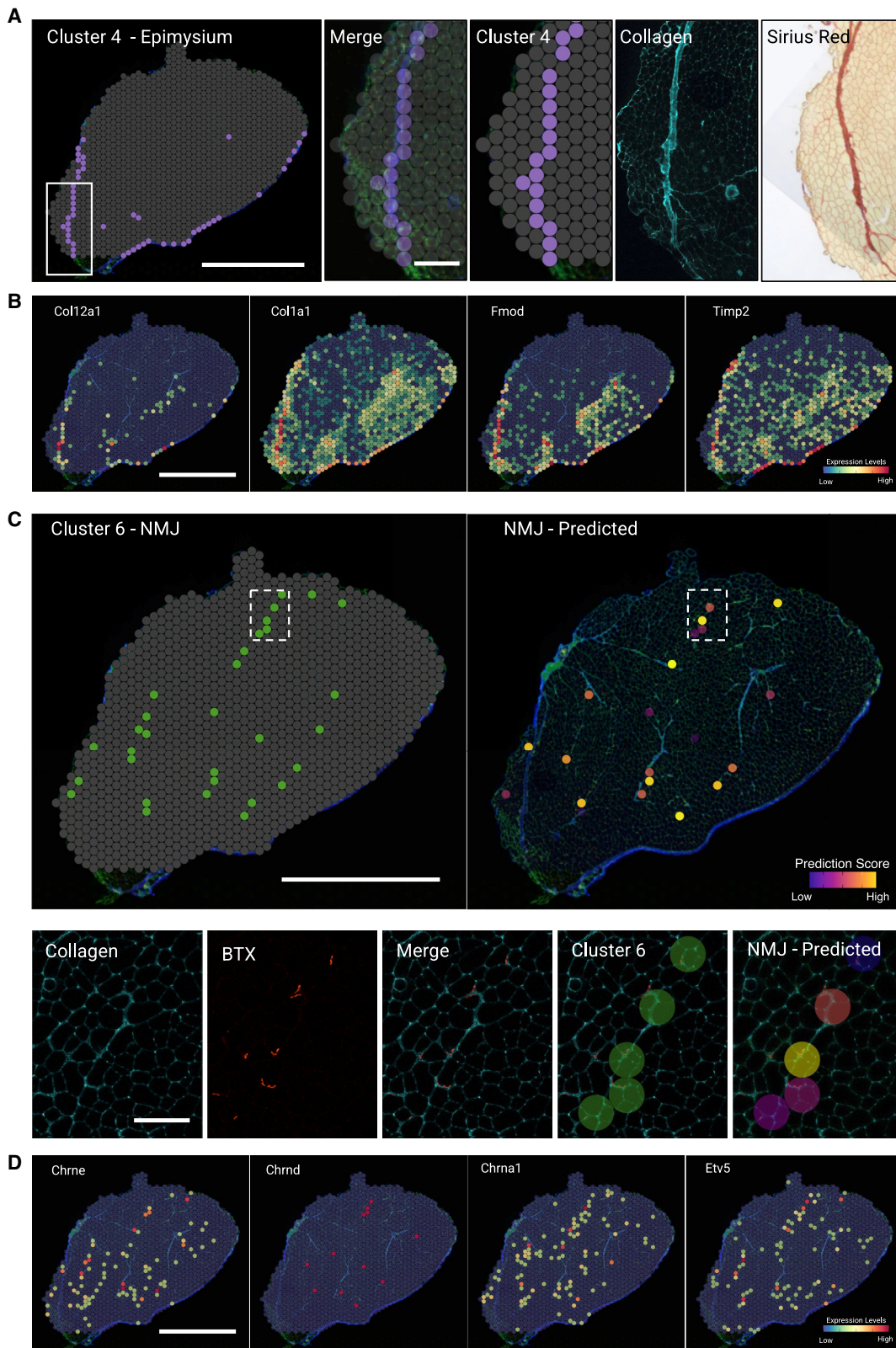
Notably, spatial gene expression data allowed the resolution of structures that are closely associated with each other anatomically. For example, clusters 5 and 7 discriminated structures attributable to nerves and vessels, respectively, even when they were located in close proximity (Figures 4C and 4D). Taken together, these data suggest that despite the relatively "large" diameter of the capturing spot (55 μm), this strategy could be used to identify the different morphofunctional domains in muscle.

Spatial transcriptome clustering analysis of transiently denervated muscle

Once we correctly annotated the different clusters in the unperturbed muscle, we proceeded to investigate their response to reversible denervation. Sciatic nerve compression is characterized by a stereotypical induction of the atrophic response that is resolved upon reinnervation.[27] Complete denervation of the TA and EDL is observed 3 days after injury (Figure S4A), as evidenced by the disappearance of synaptophysin colocalization with the BTX-positive NMJ. Reconstitution of proper

Figure 2. Cluster 0 and cluster 1 correspond to glycolytic and oxidative fibers
(A) NADH-TR staining of consecutive section (scale bar, 1 mm); cluster 0 and cluster 1 patterns display an overlap with NADH-TR low- and NADH-TR high-expressing fibers (scale bar, 2 mm).
(B) Hematoxylin and eosin staining of consecutive section (scale bar, 2 mm) illustrating muscle localization (top left) and relative expression levels of fiber-type-specific marker genes from the ST data projected over the tissue space (scale bar 2mm).
(C) Projection on the tissue space of the prediction score for 2A, 2X and 2B fibers based on snRNA-seq from WT mouse[4] integrated with ST dataset (scale bar, 2 mm).

A Cluster 4 - Epimysium | Merge | Cluster 4 | Collagen | Sirius Red

B Col12a1 | Col1a1 | Fmod | Timp2

Expression Levels
Low — High

C Cluster 6 - NMJ | NMJ - Predicted

Prediction Score
Low — High

Collagen | BTX | Merge | Cluster 6 | NMJ - Predicted

D Chrne | Chrnd | Chrna1 | Etv5

Expression Levels
Low — High

(legend on next page)

nerve-muscle interaction was observed 30 days after injury (Figure S4A). Denervation and reinnervation were also confirmed by loss and recovery of muscle mass, as shown in Figure S4B. There was also evidence of activation of the atrophic program resulting in the induction of muscle-specific ubiquitin ligases *Atrogin-1* (*Fbxo32*) and *MuRF1* (*Trim63*) in both muscles (Figure S4C). Eventually, both ubiquitin ligases will be downregulated with progressive repair and reinnervation around day 30 (Figure S4C). The averaged gene expression of the different ST timepoints recapitulated the main features of the model with an enrichment of the FoxO signaling pathway 3 days after nerve injury (Figure S4D and Table S2). In addition, we detected a peak in the expression profile of *MuRF1*, *Atrogin-1*, and several other genes known to be involved in atrophic response[28] (Figure S4E). We then analyzed the specific gene expression profile of each cluster at 3 and 30 days after denervation (Figure 5A and Table S3). Similarly, we identified the upregulation of genes related to atrophy in specific clusters such as the growth arrest and DNA damage-inducible 45α (*Gadd45a*), the ubiquitin ligase Itch (nerves), and the homeobox gene *Tgif1* (blood vessels) or autophagy-related genes beclin1 (*Becn1*) and *Gabarapl1* in both nerve and blood vessel clusters (Figure 5B). Interestingly, we noticed that the induction *Atrogin-1* and *MuRF1* were primarily localized in the glycolytic cortex of the TA muscle (Figure 5C compared with Figure 2A). In addition, 2B cluster displayed higher transcripts levels when compared with the 2A-2X cluster (Figure 5D). This observation suggests that the distribution pattern of the atrophic response depends on the muscle fiber composition, consistent with data in the literature indicating that glycolytic muscle fibers are more susceptible to muscle atrophy than oxidative muscle fibers.[29,30]

We confirmed this trend in our observations, via qPCR analysis of laser-microdissected glycolytic (Gly) or oxidative (Ox) areas of the muscle sections. *MuRF1* and *Atrogin-1* were more highly expressed in the glycolytic cortex of the denervated TA muscle than in the oxidative core (Figure S4F).

Interestingly, although the reduction in fiber cross-sectional area was rather limited at 3 days of denervation (Figure S4B), we observed, by measuring type 2A, 2X, and 2B fibers separately (representative staining shown in Figures S2D and S4G), that the reduction was significantly more pronounced in type 2B fibers than in type 2A fibers (Figure 5E). Indeed, the frequency distribution of 2B fibers reveals a reduction in the percentage of large-diameter fibers with a concomitant increase in smaller fibers following denervation. Area reduction is still visible 30 days after injury although the muscle is recovering through reinnervation. In contrast, type 2A fibers remain essentially unchanged at both 3 and 30 days after nerve damage. An intermediate phenotype was shown for type 2X fibers (Figure 5E).

Nerve-dependent polyamine synthesis-related enzyme pattern across muscle

Obtaining a detailed map of the spatial localization of specific genes in muscle could be pivotal for pinpointing new signaling pathways involved in the pathophysiology of the tissue. To this end, we screened our list of the differentially expressed genes to identify potential candidates whose expression profile was responsive to denervation both in terms of spatial and temporal regulation. Among the most enriched genes in 2B fibers in the unperturbed muscle, we identified *Amd1* (Figure 6A), a key component of the polyamine pathway (PA) (Figure S5A). Interestingly, not only *Amd1* but also other components of the PA, such as *Amd2* and *Smox*, displayed a spatial pattern reminiscent of the distribution of glycolytic fibers in the TA (Figure 6A) with a clear enrichment in the 2B fiber cluster when compared with the 2A-2X cluster (Figure 6B). As an initial finding, ST data revealed in the control (CTR) a greater expression of these genes in the TA than in the EDL (Figure 6A; see Figures 2B and S5B for EDL localization), which was confirmed by qPCR analysis (Figure 6C). After nerve crush, we observed concomitantly with a reduction in overall expression in the glycolytic cluster, a partial loss of the spatial restriction of these genes (Figures 6A and 6B). We validated this observation through laser microdissection; indeed, while the expression of *Amd1*, *Amd2*, and *Smox* was high in the glycolytic portion of the TA in control tissue, after denervation, due to their reduced expression in glycolytic fibers, the relative levels of these genes were similar between the glycolytic and oxidative fractions of the muscle (Figure 6D). Collectively these data were further validated using publicly available snRNA-seq datasets both in unperturbed TA[10,16] and in unperturbed and denervated gastrocnemius[10] (Figure S5C). It is worth mentioning that data from ST and those from laser capture, while overall overlapping, displayed some differences at 3 and 30 days after denervation. This suggests a certain degree of longitudinal intramuscular variability in the reinnervation process that can be averaged when analyzing the whole tissue (Figure 6C). Intriguingly, at 30 days after the induction of nerve damage—when innervation is restored—*Amd1*, *Amd2*, and *Smox* expression in the muscle was still decreased compared with CTR levels (Figure 6C). This could indicate that more time or more extensive maturation of NMJs is needed to re-establish the correct expression of these markers.

We speculated that such a change in expression levels could result in an imbalance in the PA pathway. The decarboxylation of S-adenosylmethionine (SAM), catalyzed by AMD1/AMD2, produces an aminopropyl group that acts as a substrate together with putrescine for the spermidine synthase to produce spermidine and subsequently to form spermine (Figure S5A). Thus, reduction of *Amd1*/*Amd2* expression may result in putrescine
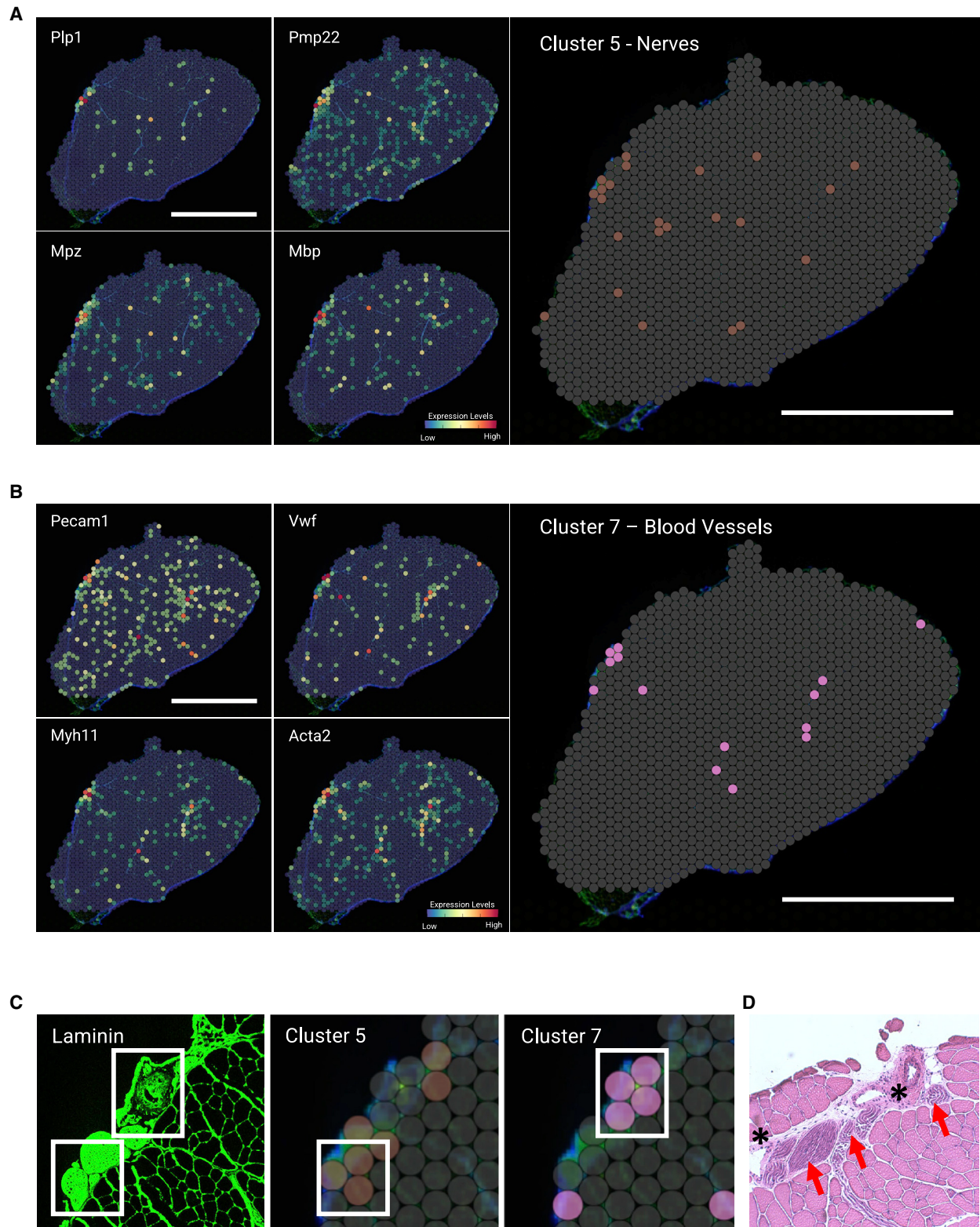

Figure 3. Cluster 4 and cluster 6 correspond to muscle perimysium and neuromuscular junction

(A) Spatial distribution of cluster 4 (left) (scale bar, 2 mm). Overlay of cluster 4 distribution over tissue space, collagen-1 staining of the region highlighted, and Sirius red staining of serial section (scale bar, 100 μm).

(B) Relative expression levels of genes enriched in cluster 4 (scale bar, 2 mm).

(C) Spatial distribution of cluster 6 (top left) and projection of prediction score for NMJ cells (top right) (scale bar, 2 mm). Enlargement of the region highlighted in the white box (bottom), immunostaining for collagen-1 and bungarotoxin respectively (left), and overlay of cluster 6 and NMJ prediction score (right) (scale bar, 100 μm).

(D) Relative expression levels of NMJ-specific marker genes from the ST data projected over the tissue space (scale bar, 2 mm).

A

Plp1

Pmp22

Cluster 5 - Nerves

Mpz

Mbp

Expression Levels
Low   High

B

Pecam1

Vwf

Cluster 7 – Blood Vessels

Myh11

Acta2

Expression Levels
Low   High

C

Laminin

Cluster 5

Cluster 7

D

(legend on next page)

accumulation. Indeed, as shown by gas chromatography-mass spectrometry (GC-MS) quantitative analysis, we observed a dramatic change in polyamine ratio 3 days after denervation (Figure 7A). A mean 25-fold increase of putrescine was revealed as a result of *Amd1* limitation. However, although their precursor was significantly increased, the amount of spermidine and spermine did not change significantly (Figure S5D). In support of this observation an induction of *Odc1*, required to synthesize putrescin from ornithine, was upregulated in denervated muscle (Figures 6B and S5E). At 30 days after nerve injury, although the expression of *Amd1*, *Amd2*, and *Smox* was not fully restored after reinnervation, the flow of the metabolic pathway was resumed, and putrescine levels were strongly downregulated (Figure 7A). To explore the possibility that putrescine accumulation is not only a consequence of denervation but may take part in the atrophic signaling and consequently amplify the muscle defect, we treated differentiated C2C12 myotubes daily with 2 mM putrescine. Interestingly, a reduction in myotube diameter was observed after 48 h of treatment (Figures 7B and 7C). Putrescine treatment shows a direct effect in inducing gene expression of *MuRF1* but not *Atrogin-1* ubiquitin ligase in myotubes compared with control myotubes (Figure 7D). Moreover, to understand whether flux alterations in polyamine production cause defects in muscle function, we conducted RNAi-mediated knockdown experiments of the CG10561 (Paox/Smox ortholog) in *Drosophila* model. To this aim, we generated a c179-GAL4>UAS-Smox^RNAi (named UAS-Smox^RNAi) to inactivate Paox/Smox ortholog expression in mesodermal-derived tissues (Figure 7E). *Drosophila* mutant showed a significative reduction of muscle function—measured in a top-climbing assay—3 and 10 days post eclosion (dpe) compared with wild-type (no UAS) animals (Figure 7F). Finally, UAS-Smox^RNAi flies showed greater fatigue than control flies after 10 repetitions of the climbing assay (Figure 7G). Altogether these data suggest that perturbations of PA homeostasis such as those occurring during reversible denervation can impact both muscle function and morphology.

DISCUSSION

Here we applied an ST Visium assay coupled with immunofluorescence to profile the transcriptional signature of distinct functional histological domains in skeletal muscle. Using a spatiotemporal analysis, we characterized their transcriptional response in a model of reversible nerve damage. Skeletal muscle is a complex organ in which the main motor unit, the fiber, is tightly interconnected with structures of different origins and heterogeneous cellular composition. Recent advances in terms of single-cell RNA sequencing have given new input to the field, enabling the unbiased transcriptomic analysis of all tissue-resident populations. However, due to the lack of positional information, 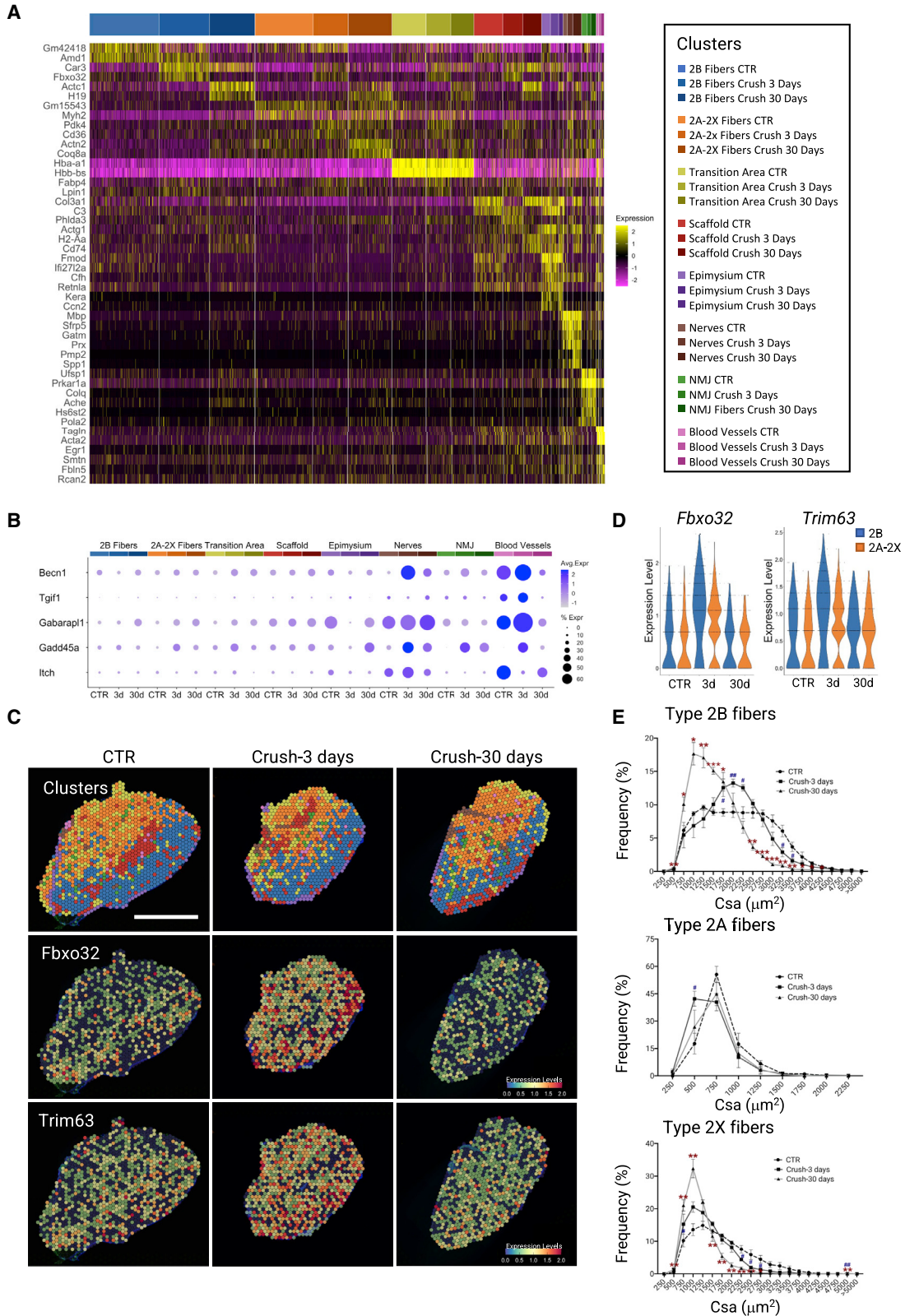current scRNA-seq and snRNA-seq methods are still unable to fully render the complexity of the different anatomical domains in muscle, ultimately providing a list of cellular components but limited insights into the coordinated activity of the whole functional unit. On the contrary, by contextualizing gene expression within its true location, ST could provide detailed information on how different structural units acts and synergize.

Indeed, our data faithfully recapitulate all the molecular events triggered by reversible nerve loss and offer a detailed temporal snapshot of the changes that occur in the different functional domains. In line with what has been extensively described in the literature, we readily detected the activation of the FoxO-mediated atrophic mechanism leading to reduced muscle mass. Furthermore, our analysis highlighted the differential activation of atrophy-related genes in specific anatomical districts. In particular, we showed that Beclin1 and Gabarapl1 are upregulated in both nerves and vessels, thus suggesting a predominant early activation of autophagy in those specific clusters. In addition, we confirmed differences in the extent of the atrophic response in oxidative vs. glycolytic fibers, with earlier and more extensive activation of *MuRF1* and *Atrogin-1* in the latter. If fiber types indeed activate distinct but consistent transcriptomic programs, differences in the atrophic response that have so far been considered intermuscular would thus likely be dependent only on the fiber type composition.[31] However, it could conversely and more intriguingly be speculated that each muscle could trigger a tailored atrophic program that is then coordinately executed by the different fiber types acting interdependently. Indeed, our data support the hypothesis that within the same muscle the specification of fibers results in a differential susceptibility to external stimuli by activating, with distinct intensities, an atrophic program in specific anatomical zones of the same muscle.

As a proof of concept that this technology can be successfully applied to skeletal muscle to identify and investigate the spatial distributions of specific signaling pathways within the tissue, we also showed how the expression of enzymes of the polyamine synthesis pathway follows a fiber metabolic gradient. In fact, genes encoding for key enzymes of this pathway tend to be more highly expressed in the glycolytic portion of the TA muscle than in the oxidative core. Furthermore, the spatial regulation of gene expression seems to be directly mediated by local innervation, since after nerve injury, we observed a loss of this gradient as a result of reduced expression of these genes in the glycolytic compartment. Moreover, the reduction of key enzymes for the conversion of putrescine into spermidine and then into spermine has the effect of dramatically accumulating putrescine in denervated muscle. In fact, the ratio between the different polyamines in the denervated muscle is perturbed, resulting in a massive accumulation of putrescine. This could be directly involved in the atrophic phenotype since while spermidine has been shown to prevent atrophy and neurodegeneration,[32–36] putrescine has

Figure 4. Cluster 5 and cluster 7 correspond to nerves and blood vessels, respectively
(A) Relative expression levels of genes enriched in cluster 5 (left). Spatial distribution of cluster 5 (right) (scale bar, 2 mm).
(B) Relative expression levels of genes enriched in cluster 7 (left). Spatial distribution of cluster 7 (right) (scale bar, 2 mm).
(C) Laminin staining of a specific region of the muscle where nerve and vessels are in close proximity. White boxes highlight the relative distribution of clusters 5 and 7 and the overlap between the anatomical structure and the transcriptomic unit.
(D) Serial section stained with hematoxylin and eosin illustrating nerve localization (red arrows) and vessel localization (asterisk).

A

Gm42418
Amd1
Car3
Fbxo32
Actc1
H19
Gm15543
Myh2
Pdk4
Cd36
Actn2
Coq8a
Hba-a1
Hbb-bs
Fabp4
Lpin1
Col3a1
C3
Phlda3
Actg1
H2-Aa
Cd74
Fmod
Ifi27l2a
Cfh
Retnla
Kera
Ccn2
Mbp
Sfrp5
Gatm
Prx
Pmp2
Spp1
Ufsp1
Prkar1a
Colq
Ache
Hs6st2
Pola2
Tagln
Acta2
Egr1
Smtn
Fbln5
Rcan2

Expression
2
1
0
-1
-2

Clusters

2B Fibers CTR
2B Fibers Crush 3 Days
2B Fibers Crush 30 Days

2A-2X Fibers CTR
2A-2x Fibers Crush 3 Days
2A-2X Fibers Crush 30 Days

Transition Area CTR
Transition Area Crush 3 Days
Transition Area Crush 30 Days

Scaffold CTR
Scaffold Crush 3 Days
Scaffold Crush 30 Days

Epimysium CTR
Epimysium Crush 3 Days
Epimysium Crush 30 Days

Nerves CTR
Nerves Crush 3 Days
Nerves Crush 30 Days

NMJ CTR
NMJ Crush 3 Days
NMJ Fibers Crush 30 Days

Blood Vessels CTR
Blood Vessels Crush 3 Days
Blood Vessels Crush 30 Days

B

2B Fibers | 2A-2X Fibers | Transition Area | Scaffold | Epimysium | Nerves | NMJ | Blood Vessels

Becn1
Tgif1
Gabarapl1
Gadd45a
Itch

Avg.Expr
2
1
0
-1

% Expr
0
10
20
30
40
50
60

CTR 3d 30d CTR 3d 30d CTR 3d 30d CTR 3d 30d CTR 3d 30d CTR 3d 30d CTR 3d 30d CTR 3d 30d

D

Fbxo32
Trim63

2B
2A-2X

Expression Level

CTR 3d 30d

C

CTR | Crush-3 days | Crush-30 days

Clusters

Fbxo32

Expression Levels
0.0 0.5 1.0 1.5 2.0

Trim63

Expression Levels
0.0 0.5 1.0 1.5 2.0

E

Type 2B fibers

Frequency (%)

Csa (μm^2)

CTR
Crush-3 days
Crush-30 days

Type 2A fibers

Frequency (%)

Csa (μm^2)

CTR
Crush-3 days
Crush-30 days

Type 2X fibers

Frequency (%)

Csa (μm^2)

CTR
Crush-3 days
Crush-30 days

(legend on next page)

been associated with neurodegenerative phenomena.[37–39] This is also supported by the observation that myotubes treated daily with putrescin display a reduction of size compared with untreated cells and a concomitant activation of *MuRF1* expression.

Although the result of the altered ratio of polyamines in denervated muscle requires specific studies, this observation corroborates the idea that innervation is required not only to support motor function, but also to regulate the gene expression profile of innervated fibers. More importantly, innervation could govern skeletal muscle functional cluster determination by driving compartmentalized transcription of specific factors. Alteration of such a regulation layer may be directly affecting muscle function and thus exacerbating atrophy. Indeed, deletion of Smox/Paox ortholog in flies results in a mobility defect, supporting the importance of proper flow in polyamine production in healthy muscle.

These events are therefore related to a distinct abundance in the expression of factors that are then prevalent in determining areas of the muscle both in basal conditions (polyamine metabolism) and after alteration of homeostasis (atrogenes). In a translational perspective, this could lead to a better understanding of how some muscle fibers are more resistant to atrophy and thus promote a shift toward this type of fiber in a therapeutic perspective.

Here, we only focused on TA and EDL muscle groups alone, which are almost exclusively composed of fast type fibers. In the future, it would be interesting to use TS to analyze atrophy in different muscle groups with a more diverse fiber composition to assess whether the same fiber types activate the same transcriptomic program in different muscles and to highlight differences with slow twitch muscle fibers (e.g., predominant in soleus muscle). In addition, exploring the regeneration process at a later time after denervation would be useful to more accurately define the molecular events that occur after nerve injury. Finally, parallel analysis of muscles undergoing nonreversible denervation would help to understand which signals are necessary to drive muscle remodeling and reinnervation and which are detrimental in mediating the catastrophic effects of innervation loss.

Recently, another spatially resolved skeletal muscle dataset has been published.[40] This dataset clearly showed the potential of a pairing of spatially resolved transcriptomics with scRNA-seq to investigate cell-cell interactions. Yet the use of hematoxylin and eosin staining as a spatial reference and the lack of a reference muscle in basal condition limited the detailed analysis of specific morphological structures. With our approach, we have achieved molecular-level discrimination of areas within the muscle with differences in metabolic activity as well as functional aggregations of finer-scale areas, such as clusters of genes restricted to the extracellular matrix, vessels, nerves, and even

muscle junctions. This enabled us to precisely detail the transcriptional signature within those anatomical clusters that would otherwise have been hidden by bulk RNA-seq or scRNA-seq. However, resolution remains a main hurdle to the potential applications of Visium technology, as each spot ideally contains one to ten cells. Several *in silico* methods have been developed to deconvolute or infer single-cell information from a single spot.[41,42–48] Nonetheless, these approaches often require scRNA-seq or bulk RNA-seq data as initial references. In muscle, the limit in resolution is partially compensated by the large size of fibers that makes the colocalization of different fibers within a single spot less likely. Eventually, the application of denser spot arrays or different technological strategies can overcome this technical bottleneck and open the way to the characterization of subcellular transcripts localization at the whole genome level. It should nonetheless be taken into account that these ultra-resolution approaches require advanced segmentation strategies in order to correctly assign each transcript to its cell. This will be particularly interesting, and potentially challenging, in skeletal muscle where large multinucleated cells, such as the myofibers, coexist with a very diverse and compacted fraction of mononuclear cells.

Despite the current limitations, we foresee that the use of ST technologies will be instrumental in understanding the molecular dynamics occurring at the local level, such as stem cell-niche interactions and, by clarifying where a particular event occurs in terms of tissue localization, will contribute elucidating the response of specific histological functional units to external perturbations such as traumatic injury or chronic inflammatory conditions.
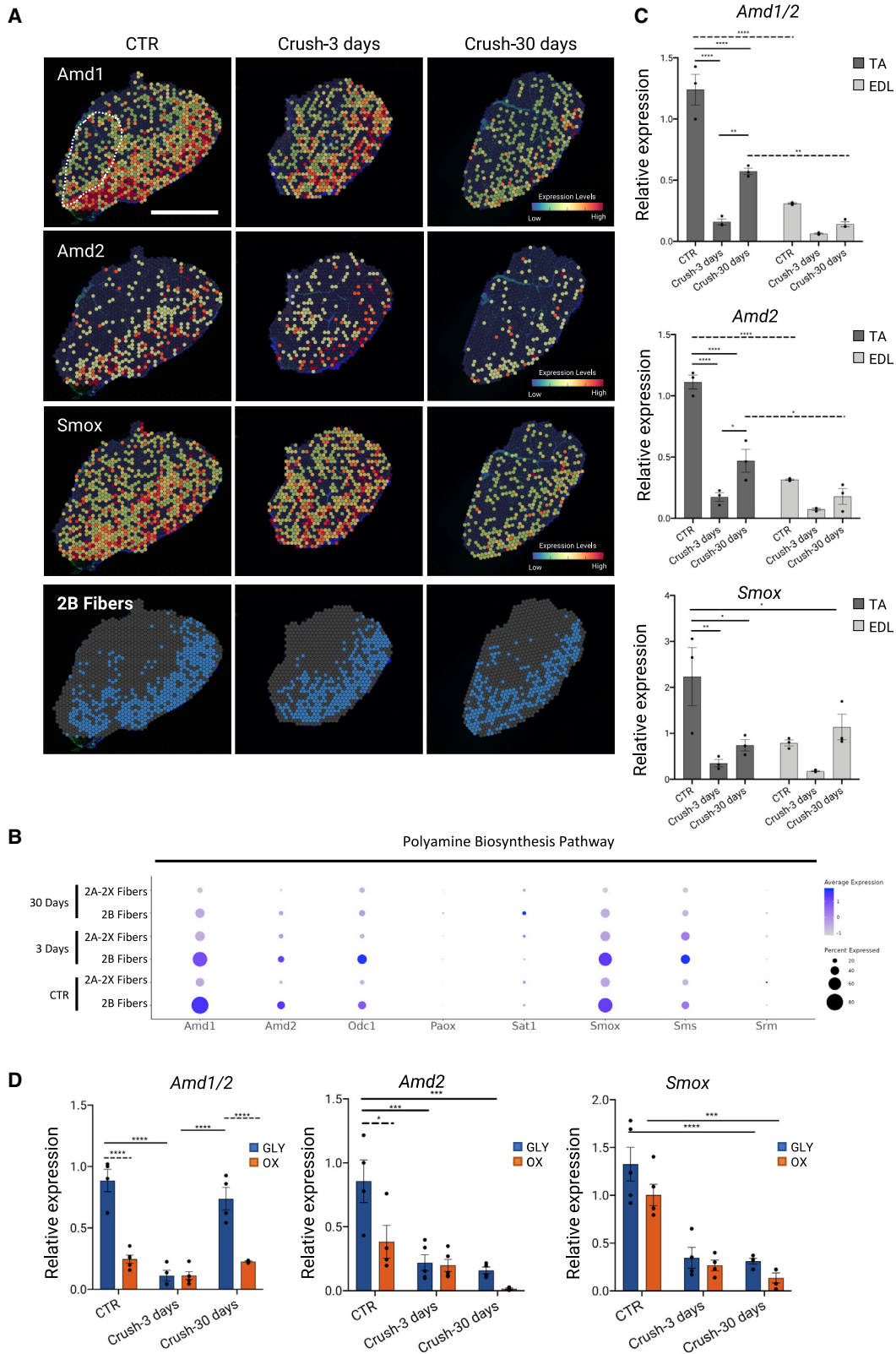
In summary, our study provides a detailed molecular profiling that will serve as a steppingstone to investigate the mechanism underpinning muscle-specific response to denervation at a morphofunctional level as in the case of differential fiber sensitivity to atrophy. Furthermore, providing a spatially resolved transcriptomic reference of the unperturbed muscle will allow the identification of new cellular or structural interactions in response to any perturbation of the homeostatic balance.

Limitations of the study

In our study we relied on already published datasets[4,10,16] to confirm our findings, and we did not perform any additional snRNA-seq to match our timepoints after reversible denervation; as a consequence, we were not able to perform spot deconvolution. Furthermore, due to the relative size of each spot, the resulting gene expression is an average of multiple cells, so more homogeneous areas tend to display a stronger signature. As an example, in the EDL, despite being largely composed of

Figure 5. ST reveals discrete dynamics during denervation-induced atrophy

(A) Heatmap showing expression values of the two most variable genes for each cluster in each time point after differential gene expression analysis.

(B) Dot plot illustrating the relative expression and distribution of the cluster-specific atrophy genes.

(C) Cluster distribution and relative expression levels of *Fbox32* and *Trim63* transcripts during denervation-reinnervation process (scale bar, 2 mm).

(D) Violin plot showing the expression of *Fbox32* and *Trim63* in glycolytic and oxidative fibers clusters.

(E) Frequency distribution of fiber's cross-section area (CSA) of type 2A, 2B, and 2X muscle fibers. CTR values (circle), crush-3 days values (square), crush-30 days values (triangle) (n = 3 for CTR, n = 4 denervated [crush-3 and crush-30 days]); blue hash denotes p value between CTR and crush-3 days; red asterisk denotes p value between CTR and crush-30 days; values represent mean ± standard error of the mean (SEM), * or # $p < 0.05$, ** or ## $p < 0.01$, *** or ### $p < 0.001$, by unpaired two-tailed t test.

A
CTR | Crush-3 days | Crush-30 days

Amd1
Amd2
Smox
2B Fibers

C
Amd1/2
Amd2
Smox

B
Polyamine Biosynthesis Pathway

30 Days — 2A-2X Fibers / 2B Fibers
3 Days — 2A-2X Fibers / 2B Fibers
CTR — 2A-2X Fibers / 2B Fibers

Amd1 Amd2 Odc1 Paox Sat1 Smox Sms Srm

D
Amd1/2
Amd2
Smox

(legend on next page)

type 2B fibers, the relative detected intensity of Myh4 is lower compared with the large glycolytic area in the TA. This is most likely due to the fact that in the EDL different fiber types do not exhibit a marked spatial segregation. Consequently, within the same spot are averaged fibers of different types, thus resulting in an overall dampening of relative expression of the distinct specific genes. Another limitation is that our dataset focuses only on TA and EDL, and although snRNA-seq data from Lin et al.[10] suggest that similar events occur in the gastrocnemius, we cannot rule out that in other muscles some of the polyamine pathway genes could have a different spatial distribution.

STAR★METHODS

Detailed methods are provided in the online version of this paper and include the following:

- KEY RESOURCES TABLE
- RESOURCE AVAILABILITY
  - Lead contact
  - Materials availability
  - Data and code availability
- EXPERIMENTAL MODEL AND SUBJECT DETAILS
  - Mouse lines
- METHOD DETAILS
  - Denervation
  - Spatial RNA sequencing library preparation
  - Laser microdissection
  - RNA analysis by quantitative PCR
  - Histological staining
  - C2.C12 culture
  - Drosophila strains and rearing conditions
  - Climbing assays
  - Polyamine analysis
  - Western Blot
  - Figure design
- QUANTIFICATION AND STATISTICAL ANALYSIS
  - Statistical analysis

SUPPLEMENTAL INFORMATION

Supplemental information can be found online at https://doi.org/10.1016/j.celrep.2022.111861.

AUTHOR CONTRIBUTIONS

M.L and G.L designed experiments and analyzed results. D.C., D.P., R.V., P.D., V.L., P.C., C.S.R., and R.A. performed and analyzed experiments. B.D. and S.C. designed and performed microdissection experiments. A.M. performed polyamine quantification experiments. M.M. and C.L. designed and performed Drosophila-related experiments. M.L. and G.L wrote the manuscript.

REFERENCES

1. Oprescu, S.N., Yue, F., Qiu, J., Brito, L.F., and Kuang, S. (2020). Temporal dynamics and heterogeneity of cell populations during skeletal muscle regeneration. iScience 23, 100993. https://doi.org/10.1016/j.isci.2020.100993.

2. Liu, W., and Chakkalakal, J.v. (2018). The composition, development, and regeneration of neuromuscular junctions. Curr. Top. Dev. Biol. 126, 99–124. https://doi.org/10.1016/BS.CTDB.2017.08.005.

3. Sartori, R., Romanello, V., and Sandri, M. (2021). Mechanisms of muscle atrophy and hypertrophy: implications in health and disease. Nat. Commun. 12, 330. https://doi.org/10.1038/S41467-020-20123-1.

4. Chemello, F., Wang, Z., Li, H., McAnally, J.R., Liu, N., Bassel-Duby, R., and Olson, E.N. (2020). Degenerative and regenerative pathways underlying Duchenne muscular dystrophy revealed by single-nucleus RNA sequencing. Proc. Natl. Acad. Sci. USA 117, 29691–29701. https://doi.org/10.1073/PNAS.2018391117.

5. De Micheli, A.J., Laurilliard, E.J., Heinke, C.L., Ravichandran, H., Fraczek, P., Soueid-Baumgarten, S., de Vlaminck, I., Elemento, O., and Cosgrove, B.D. (2020). Single-cell analysis of the muscle stem cell hierarchy identifies heterotypic communication signals involved in skeletal muscle regeneration. Cell Rep. 30, 3583–3595.e5. https://doi.org/10.1016/J.CELREP.2020.02.067.

6. Dell'Orso, S., Juan, A.H., Ko, K.-D., Naz, F., Perovanovic, J., Gutierrez-Cruz, G., Feng, X., and Sartorelli, V. (2019). Single cell analysis of adult mouse skeletal muscle stem cells in homeostatic and regenerative conditions. Development 146, dev174177. https://doi.org/10.1242/dev.174177.

7. Dos Santos, M., Backer, S., Saintpierre, B., Izac, B., Andrieu, M., Letourneur, F., Relaix, F., Sotiropoulos, A., and Maire, P. (2020). Single-nucleus RNA-seq and FISH identify coordinated transcriptional activity in mammalian myofibers. Nat. Commun. 11, 5102–5116. https://doi.org/10.1038/s41467-020-18789-8.

8. Giordani, L., He, G.J., Negroni, E., Sakai, H., Law, J.Y.C., Siu, M.M., Wan, R., Corneau, A., Tajbakhsh, S., Cheung, T.H., and Le Grand, F. (2019).

Figure 6. ST identifies innervation dependent pathways
(A) Cluster 0 distribution and relative expression levels of spermidine pathway component (Amd1, Amd2, and Smox); scale bar, 2 mm (dotted line highlights EDL muscle).
(B) Dotplot illustrating the relative expression and distribution of the spermidine pathway.
(C) Relative expression of Amd1/2, Amd2, and Smox during denervation in TA and EDL muscle (n = 3, values represent mean ± SEM, *p < 0.05, **p < 0.01,***p < 0.001, ****p < 0.0001, by two-way ANOVA Tukey's multiple-comparison test).
(D) Relative expression of Amd1, Amd2, and Smox after laser microdissection of TA 3 days and 30 days after denervation (n > 4, values represent mean ± SEM, *p < 0.05, **p < 0.01,***p < 0.001, ****p < 0.0001, by one-way ANOVA Tukey's multiple-comparison test).
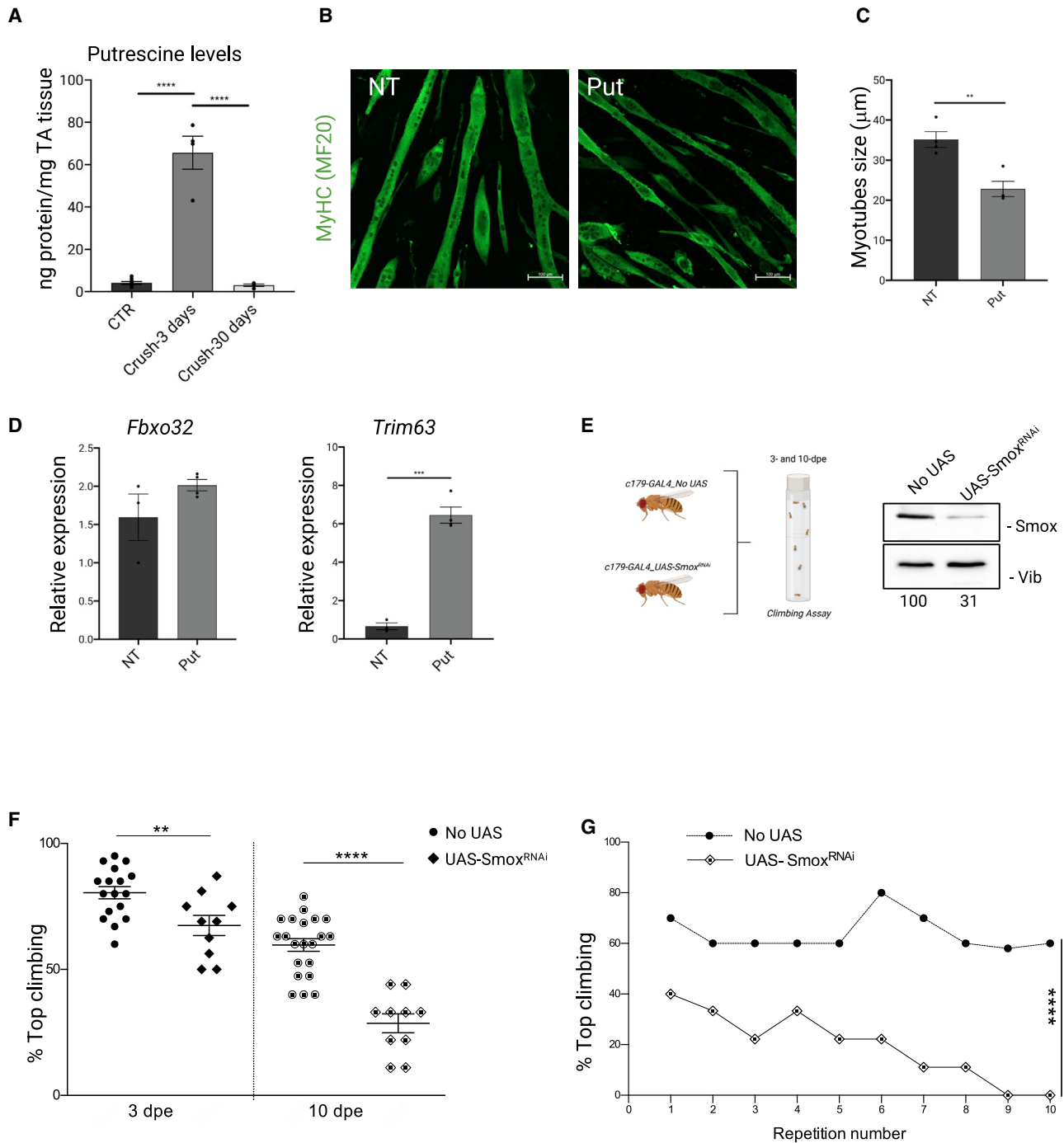
A

B

C

D

E

F

G

Figure 7. Alterations in polyamine homeostasis affect muscle size and function

(A) GC-MS quantitative analysis of putrescine levels in control (CTR) and denervated (crush-3 and crush-30 days) muscles (n = 8 CTR, n = 4 denervated [crush-3 and crush-30 days]; values represent mean ± SEM by ****p < 0.0001, by unpaired two-tailed t test).

(B) Representative immunostaining for myosin heavy chain (MyHC-MF20) (green) on myotubes treated with 2 mM of putrescine (Put) for 48 h (scale bar, 100 μm).

(C) Mean of myotubes diameter; 27% is the decrease of treatment respect to untreated (NT) (n = 4, values represent mean ± SEM, **p < 0.01, by unpaired two-tailed t test).

(D) Relative expression of *Fbxo32* and *Trim63* in C2C12 myotubes treated with 2 mM putrescine (Put) for 48 h (n = 3 for NT and n = 4 Put; values represent mean ± SEM, ***p < 0.001, by unpaired two-tailed t test).

(E) Experimental workflow (left). Western blot on larval extracts obtained from control (no UAS) or interfered *UAS-Smox^RNA* individuals under the control of the *C179-GAL4* driver. Numbers below represent band quantification normalized on loading control (Vib).

(legend continued on next page)

High-dimensional single-cell cartography reveals novel skeletal muscle-resident cell populations. Mol. Cell *74*, 609–621.e6. https://doi.org/10.1016/j.molcel.2019.02.026.

9. Kim, M., Franke, V., Brandt, B., Lowenstein, E.D., Schöwel, V., Spuler, S., Akalin, A., and Birchmeier, C. (2020). Single-nucleus transcriptomics reveals functional compartmentalization in syncytial skeletal muscle cells. Nat. Commun. *11*, 6375. https://doi.org/10.1038/s41467-020-20064-9.

10. Lin, H., Ma, X., Sun, Y., Peng, H., Wang, Y., Thomas, S.S., and Hu, Z. (2022). Decoding the transcriptome of denervated muscle at single-nucleus resolution. J. Cachexia Sarcopenia Muscle *13*, 2102–2117. https://doi.org/10.1002/JCSM.13023.

11. Nicoletti, C., Wei, X., Etxaniz, U., Proietti, D., Madaro, L., Puri, P.L., Puri, P.L., Development, M.D., Program, R., and Burnham, S. (2020). scRNA-seq-based analysis of skeletal muscle response to denervation reveals selective activation of muscle-resident glial cells and fibroblasts. Preprint at bioRxiv. https://doi.org/10.1101/2020.12.29.424762.

12. Petrilli, L.L., Spada, F., Fuoco, C., Micarelli, E., Reggio, A., Rosina, M., Gargioli, C., Castagnoli, L., and Cesareni, G. (2017). Single-cell quantitative analysis of skeletal muscle cell population dynamics during regeneration and ageing. Preprint at bioRxiv. https://doi.org/10.1101/222158.

13. Proietti, D., Giordani, L., de Bardi, M., D'Ercole, C., Lozanoska-Ochser, B., Amadio, S., Volonté, C., Marinelli, S., Muchir, A., Bouché, M., et al. (2021). Activation of skeletal muscle-resident glial cells upon nerve injury. JCI Insight *6*, e143469. https://doi.org/10.1172/jci.insight.143469.

14. Rubenstein, A.B., Smith, G.R., Raue, U., Begue, G., Minchev, K., Ruf-Zamojski, F., Nair, V.D., Wang, X., Zhou, L., Zaslavsky, E., et al. (2020). Single-cell transcriptional profiles in human skeletal muscle. Sci. Rep. *10*, 229. https://doi.org/10.1038/s41598-019-57110-6.

15. Tabula Muris Consortium, Overall coordination, Logistical coordination, Organ collection and processing, Library preparation and sequencing, Computational data analysis, Cell type annotation, Writing group, Supplemental text writing group, Principal investigators, et al. (2018). Single-cell transcriptomics of 20 mouse organs creates a Tabula Muris. Nature *562*, 367-372. 10.1038/s41586-018-0590-4.

16. Petrany, M.J., Swoboda, C.O., Sun, C., Chetal, K., Chen, X., Weirauch, M.T., Salomonis, N., and Millay, D.P. (2020). Single-nucleus RNA-seq identifies transcriptional heterogeneity in multinucleated skeletal myofibers. Nat. Commun. *11*, 6374–6412. https://doi.org/10.1038/s41467-020-20063-w.

17. Achim, K., Pettit, J.B., Saraiva, L.R., Gavriouchkina, D., Larsson, T., Arendt, D., and Marioni, J.C. (2015). High-throughput spatial mapping of single-cell RNA-seq data to tissue of origin. Nat. Biotechnol. *33*, 503–509. https://doi.org/10.1038/NBT.3209.

18. Hunter, M.v., Moncada, R., Weiss, J.M., Yanai, I., and White, R.M. (2021). Spatially resolved transcriptomics reveals the architecture of the tumor-microenvironment interface. Nat. Commun. *12*, 6278–6316. https://doi.org/10.1038/s41467-021-26614-z.

19. Ji, A.L., Rubin, A.J., Thrane, K., Jiang, S., Reynolds, D.L., Meyers, R.M., Guo, M.G., George, B.M., Mollbrink, A., Bergenstråhle, J., et al. (2020). Multimodal analysis of composition and spatial architecture in human squamous cell carcinoma. Cell *182*, 1661–1662. https://doi.org/10.1016/J.CELL.2020.08.043.

20. Rao, A., Barkley, D., França, G.S., and Yanai, I. (2021). Exploring tissue architecture using spatial transcriptomics. Nature *596*, 211–220. https://doi.org/10.1038/s41586-021-03634-9.

21. Hagiwara, N., Yeh, M., and Liu, A. (2007). Sox6 is required for normal fiber type differentiation of fetal skeletal muscle in mice. Dev. Dynam. *236*, 2062–2076. https://doi.org/10.1002/DVDY.21223.

22. Lee, K.Y., Singh, M.K., Ussar, S., Wetzel, P., Hirshman, M.F., Goodyear, L.J., Kispert, A., and Kahn, C.R. (2015). Tbx15 controls skeletal muscle fibre-type determination and muscle metabolism. Nat. Commun. *6*, 8054. https://doi.org/10.1038/NCOMMS9054.

23. Meng, Z.X., Li, S., Wang, L., Ko, H.J., Lee, Y., Jung, D.Y., Okutsu, M., Yan, Z., Kim, J.K., and Lin, J.D. (2013). BAF60c drives glycolytic muscle formation and improves glucose homeostasis through Deptor-mediated AKT activation. Nat. Med. *19*, 640–645. https://doi.org/10.1038/NM.3144.

24. Reyes, N.L., Banks, G.B., Tsang, M., Margineantu, D., Gu, H., Djukovic, D., Chan, J., Torres, M., Liggitt, H.D., Hirenallur-S, D.K., et al. (2015). Fnip1 regulates skeletal muscle fiber type specification, fatigue resistance, and susceptibility to muscular dystrophy. Proc. Natl. Acad. Sci. USA *112*, 424–429. https://doi.org/10.1073/PNAS.1413021112/SUPPL_FILE/PNAS.201413021SI.PDF.

25. Wiederstein, J.L., Nolte, H., Günther, S., Piller, T., Baraldo, M., Kostin, S., Bloch, W., Schindler, N., Sandri, M., Blaauw, B., et al. (2018). Skeletal muscle-specific methyltransferase METTL21C trimethylates p97 and regulates autophagy-associated protein breakdown. Cell Rep. *23*, 1342–1356. https://doi.org/10.1016/J.CELREP.2018.03.136.

26. Schiaffino, S., and Reggiani, C. (2011). Fiber types in Mammalian skeletal muscles. Physiol. Rev. *91*, 1447–1531. https://doi.org/10.1152/physrev.00031.2010.

27. Magill, C.K., Tong, A., Kawamura, D., Hayashi, A., Hunter, D.A., Parsadanian, A., Mackinnon, S.E., and Myckatyn, T.M. (2007). Reinnervation of the tibialis anterior following sciatic nerve crush injury: a confocal microscopic study in transgenic mice. Exp. Neurol. *207*, 64–74. https://doi.org/10.1016/j.expneurol.2007.05.028.

28. Milan, G., Romanello, V., Pescatore, F., Armani, A., Paik, J.-H., Frasson, L., Seydel, A., Zhao, J., Abraham, R., Goldberg, A.L., et al. (2015). Regulation of autophagy and the ubiquitin–proteasome system by the FoxO transcriptional network during muscle atrophy. Nat. Commun. *6*, 6670. https://doi.org/10.1038/ncomms7670.

29. De Theije, C.C., Langen, R.C.J., Lamers, W.H., Gosker, H.R., Schols, A.M.W.J., and Köhler, S.E. (2015). Differential sensitivity of oxidative and glycolytic muscles to hypoxia-induced muscle atrophy. J. Appl. Physiol. *118*, 200–211. https://doi.org/10.1152/japplphysiol.00624.2014.

30. Wang, Y., and Pessin, J.E. (2013). Mechanisms for fiber-type specificity of skeletal muscle atrophy. Curr. Opin. Clin. Nutr. Metab. Care *16*, 243–250. https://doi.org/10.1097/MCO.0B013E328360272D.

31. Brocca, L., Toniolo, L., Reggiani, C., Bottinelli, R., Sandri, M., and Pellegrino, M.A. (2017). FoxO-dependent atrogenes vary among catabolic conditions and play a key role in muscle atrophy induced by hindlimb suspension. J. Physiol. *595*, 1143–1158. https://doi.org/10.1113/JP273097.

32. Clarkson, A.N., Liu, H., Pearson, L., Kapoor, M., Harrison, J.C., Sammut, I.A., Jackson, D.M., and Appleton, I. (2004). Neuroprotective effects of spermine following hypoxic-ischemic-induced brain damage: a mechanistic study. Faseb. J. *18*, 1114–1116. https://doi.org/10.1096/FJ.03-1203FJE.

33. Coni, S., Falconio, F.A., Marzullo, M., Munafò, M., Zuliani, B., Mosti, F., Fatica, A., Ianniello, Z., Bordone, R., Macone, A., et al. (2021). Translational control of polyamine metabolism by CNBP is required for Drosophila locomotor function. Elife *10*, e69269. https://doi.org/10.7554/ELIFE.69269.

34. Noro, T., Namekata, K., Kimura, A., Guo, X., Azuchi, Y., Harada, C., Nakano, T., Tsuneoka, H., and Harada, T. (2015). Spermidine promotes retinal ganglion cell survival and optic nerve regeneration in adult mice following optic nerve injury. Cell Death Dis. *6*, e1720. https://doi.org/10.1038/CDDIS.2015.93.

35. Noro, T., Namekata, K., Azuchi, Y., Kimura, A., Guo, X., Harada, C., Nakano, T., Tsuneoka, H., and Harada, T. (2015). Spermidine ameliorates

(F) Climbing assay performed in adult flies expressing either *UAS-Smox^RNAi* (filled and spotted diamonds), or no UAS as control (filled and spotted circles) at 3 or 10 dpe (values represent mean ± SEM; ****p > 0.0001, **p > 0.01, in unpaired t test).

(G) Fatigue assay performed in the same 10 dpe adult flies shown in (F). n ≥ 30 animals for each genotype. Asterisks represent the significance of the simple linear regression in R squared test; ****p > 0.0001.

neurodegeneration in a mouse model of normal tension glaucoma. Invest. Ophthalmol. Vis. Sci. *56*, 5012–5019. https://doi.org/10.1167/IOVS.15-17142.

36. Sharma, S., Kumar, P., and Deshmukh, R. (2018). Neuroprotective potential of spermidine against rotenone induced Parkinson's disease in rats. Neurochem. Int. *116*, 104–111. https://doi.org/10.1016/J.NEUINT.2018.02.010.

37. Camón, L., de Vera, N., and Martínez, E. (2001). Polyamine metabolism and glutamate receptor agonists-mediated excitotoxicity in the rat brain. J. Neurosci. Res. *66*, 1101–1111. https://doi.org/10.1002/JNR.10024.

38. Plewa, S., Poplawska-Domaszewicz, K., Florczak-Wyspianska, J., Klupczynska-Gabryszak, A., Sokol, B., Miltyk, W., Jankowski, R., Kozubski, W., Kokot, Z.J., and Matysiak, J. (2021). The metabolomic approach reveals the alteration in human serum and cerebrospinal fluid composition in Parkinson's disease patients. Pharmaceuticals *14*, 935. https://doi.org/10.3390/PH14090935.

39. Virgili, M., Crochemore, C., Peña-Altamira, E., and Contestabile, A. (2006). Regional and temporal alterations of ODC/polyamine system during ALS-like neurodegenerative motor syndrome in G93A transgenic mice. Neurochem. Int. *48*, 201–207. https://doi.org/10.1016/J.NEUINT.2005.10.004.

40. McKellar, D.W., Walter, L.D., Song, L.T., Mantri, M., Wang, M.F.Z., de Vlaminck, I., and Cosgrove, B.D. (2021). Large-scale integration of single-cell transcriptomic data captures transitional progenitor states in mouse skeletal muscle regeneration. Commun. Biol. *4*, 1280–1312. https://doi.org/10.1038/s42003-021-02810-x.

41. Hao, Y., Hao, S., Andersen-Nissen, E., Mauck, W.M., Zheng, S., Butler, A., Lee, M.J., Wilk, A.J., Darby, C., Zager, M., et al. (2021). Integrated analysis of multimodal single-cell data. Cell *184*, 3573–3587.e29. https://doi.org/10.1016/J.CELL.2021.04.048.

42. Andersson, A., Bergenstråhle, J., Asp, M., Bergenstråhle, L., Jurek, A., Fernández Navarro, J., and Lundeberg, J. (2020). Single-cell and spatial transcriptomics enables probabilistic inference of cell type topography. Commun. Biol. *3*, 565–568. https://doi.org/10.1038/s42003-020-01247-y.

43. Cable, D.M., Murray, E., Zou, L.S., Goeva, A., Macosko, E.Z., Chen, F., and Irizarry, R.A. (2022). Robust decomposition of cell type mixtures in spatial transcriptomics. Nat. Biotechnol. *40*, 517–526. https://doi.org/10.1038/s41587-021-00830-w.

44. Dong, R., and Yuan, G.C. (2021). SpatialDWLS: accurate deconvolution of spatial transcriptomic data. Genome Biol. *22*, 145. https://doi.org/10.1186/S13059-021-02362-7.

45. Elosua-Bayes, M., Nieto, P., Mereu, E., Gut, I., and Heyn, H. (2021). SPOTlight: seeded NMF regression to deconvolute spatial transcriptomics spots with single-cell transcriptomes. Nucleic Acids Res. *49*, E50. https://doi.org/10.1093/NAR/GKAB043.

46. Sun, D., Liu, Z., Li, T., Wu, Q., and Wang, C. (2022). STRIDE: accurately decomposing and integrating spatial transcriptomics using single-cell RNA sequencing. Nucleic Acids Res. *50*, e42. https://doi.org/10.1093/NAR/GKAC150.

47. Wang, P., Tang, W., Li, Z., Zou, Z., Zhou, Y., Li, R., Xiong, T., Wang, J., and Zou, P. (2019). Mapping spatial transcriptome with light-activated proximity-dependent RNA labeling. Nat. Chem. Biol. *15*, 1110–1119. https://doi.org/10.1038/S41589-019-0368-5.

48. Zhao, E., Stone, M.R., Ren, X., Guenthoer, J., Smythe, K.S., Pulliam, T., Williams, S.R., Uytingco, C.R., Taylor, S.E.B., Nghiem, P., et al. (2021). Spatial transcriptomics at subspot resolution with BayesSpace. Nat. Biotechnol. *39*, 1375–1384. https://doi.org/10.1038/s41587-021-00935-2.

49. Porrazzo, A., Cipressa, F., de Gregorio, A., De Pittà, C., Sales, G., Ciapponi, L., Morciano, P., Esposito, G., Tabocchini, M.A., and Cenci, G. (2022). Low dose rate γ-irradiation protects fruit fly chromosomes from double strand breaks and telomere fusions by reducing the esi-RNA biogenesis factor Loquacious. Commun. Biol. *5*, 905–912. https://doi.org/10.1038/s42003-022-03885-w.

50. Schneider, C.A., Rasband, W.S., and Eliceiri, K.W. (2012). NIH Image to ImageJ: 25 years of image analysis. Nat. Methods *9*, 671–675. https://doi.org/10.1038/nmeth.2089.

51. Wickham, H., François, R., Henry, L., and Müller, K. (2022). Dplyr: A Grammar of Data Manipulation. https://dplyr.tidyverse.org. https://github.com/tidyverse/dplyr.

52. Wilke, C., Fox, S.J., Bates, T., Manalo, K., Lang, B., Barrett, M., Stoiber, M., Philipp, A., Denney, B., Hesselberth, J., et al. (2021). Wilkelab/Cowplot: 1.1.1 (1.1.1) (Zenodo). https://doi.org/10.5281/zenodo.4411966.

53. Wickham, H. (2016). Data Analysis, pp. 189–201. https://doi.org/10.1007/978-3-319-24277-4_9.

54. Hafemeister, C., and Satija, R. (2019). Normalization and variance stabilization of single-cell RNA-seq data using regularized negative binomial regression. Genome Biol. *20*, 296. https://doi.org/10.1186/S13059-019-1874-1.

55. Pedersen, T. (2022). Patchwork: The Composer of Plots. https://patchwork.data-imaginist.com. https://github.com/thomasp85/patchwork.

56. Garnier, S., Ross, N., Budis, B., Filipovic-Pierucci, A., Galili, T., Greenwell, B., Sievert, C., Harris, D.J., Sciaini, M., and Chen., J.J. (2021). Sjmgarnier/Viridis: CRAN release v0.6.2 (v0.6.2CRAN) (Zenodo). https://doi.org/10.5281/zenodo.5579397.

57. Peterson, H., Kolberg, L., Raudvere, U., Kuzmin, I., and Vilo, J. (2020). gprofiler2 – an R package for gene list functional enrichment analysis and namespace conversion toolset g: Profiler. F1000Res *9*. https://doi.org/10.12688/F1000RESEARCH.24956.2/.

58. McGinnis, C.S., Murrow, L.M., and Gartner, Z.J. (2019). DoubletFinder: doublet detection in single-cell RNA sequencing data using artificial nearest neighbors. Cell Syst. *8*, 329–337.e4. https://doi.org/10.1016/J.CELS.2019.03.003.

59. Pau, G., Fuchs, F., Sklyar, O., Boutros, M., and Huber, W. (2010). EBImage—an R package for image processing with applications to cellular phenotypes. Bioinformatics *26*, 979–981. https://doi.org/10.1093/BIOINFORMATICS/BTQ046.

60. Kuleshov, M.v., Jones, M.R., Rouillard, A.D., Fernandez, N.F., Duan, Q., Wang, Z., Koplev, S., Jenkins, S.L., Jagodnik, K.M., Lachmann, A., et al. (2016). Enrichr: a comprehensive gene set enrichment analysis web server 2016 update. Nucleic Acids Res. *44*, W90–W97. https://doi.org/10.1093/NAR/GKW377.

STAR★METHODS

KEY RESOURCES TABLE

REAGENT or RESOURCE	SOURCE	IDENTIFIER
Antibodies		
Anti-Laminin (1:200 for IF)	Sigma-Aldrich	Cat #L9393; RRID:AB_477163
Anti-Col1A (COL-1) (1:200 for IF)	Santa Cruz Biotecnology	Cat #sc-59772;RRID:AB_1121787
Anti-Synaptophysin Polyclonal Antibody (1:300 for IF)	Invitrogen	Cat # PA1-1043
Anti-Myosin (1:20 for IF)	DSHB	N/A
Myosin heavy chain, Type 2B BF-F3 (1:50 for IF)	DSHB	N/A
Myosin heavy chain, Type 2A 2F7 (1:10 for IF)	DSHB	N/A
Anti-Smox (1:250 for WB)	Thermo Fisher Scientific	SMOX-101AP
Anti-Giotto (Vibrator, Vib)	Porazzo et al.[49]	N/A
Goat anti-Mouse IgM Alexa Flour 555 (1:200 for IF)	Invitrogen	Cat # A-21426; RRID:AB_2535847
Goat anti-Mouse IgG(H + L) Alexa Flour 594 (1:200 for IF)	Invitrogen	Cat # A-21235
Goat anti-Mouse IgG(H + L) Alexa Flour 488 (1:200 for IF)	Invitrogen	Cat # A-11001
Goat anti-Rabbit IgG(H + L) Alexa Flour 647 (1:200 for IF)	Invitrogen	Cat # A-21244
Goat anti-Rabbit IgG(H + L) Alexa Flour 594 (1:200 for IF)	Invitrogen	Cat #A-11012
Chemicals, peptides, and recombinant proteins		
Tissue-Tek OCT Compound	VWR	Cat # 361603E
2-Methylbutane	Sigma Aldrich	Cat # 27, 034–2
SSC Buffer 20x Concentration	Millipore Sigma	Cat #S6639L
Triton X-100 Solution, ~10% in H_2O	Sigma Aldrich	Cat # 93443–100ML
RiboLock RNase Inhibitor	Thermo Fisher	Cat # EO0382
Ribonucleoside Vanadyl Complex (200 mM)	Sigma Aldrich	Cat #R3380
Tris 1M, pH 7.0, RNase-free	Thermo Fisher Scientific	Cat # AM9850G
Low TE Buffer (10 mM Tris-HCl pH 8.0, 0.1 mM EDTA)	Thermo Fisher Scientific	Cat # 12090–015
Hydrochloric Acid Solution, 0.1N	Fisher Chemical	Cat # SA54-1
Methanol, for HPLC, ≥99.9%	Millipore Sigma	Cat # 34860
Qiagen Buffer EB	Qiagen	Cat #19086
DAPI	Invitrogen- Thermo Fisher Scientific	Cat #D1306
a-bungarotoxin, Alexa Fluor 488 (1:200 for IF)	Invitrogen- Thermo Fisher Scientific	Cat #B13422
Zoletil 50	Virbac	N/A
Rompum	BAYER	N/A
Tamoxifen	Sigma	Cat #T5648
β-Mercaptoethoethanol	Sigma Aldrich	Cat #M3148
UltraPure™ DNase/RNase-Free Distilled Water	Life Technologies	Cat # 10977–035
Ethanol	Sigma Aldrich	Cat #02851

Continued

REAGENT or RESOURCE	SOURCE	IDENTIFIER
NADH (disodium salt, approx 100% grade)	Roche	Cat #10107735001
NBT (4-Nitro blue tetrazolium chloride)	Roche	Cat #11087479001
Eosin Y solution alcoholic	Sigma Aldrich	Cat #HT110332
Harris Hematoxylin Solution, Modified	Sigma Aldrich	Cat #HHS32
Bouin's solution	Sigma Aldrich	Cat #HT10132
Diret Red 80	Sigma Aldrich	Cat #365548
Acetic acid glacial	Scharlau	Cat #AC03442500
Albumin (BSA) Fraction V (pH 7.0)	PanReac AppliChem	Cat #A1391,0100
PBS tablets pH 7.4	PanReac AppliChem	Cat #A9201,0010
Eukitt Quick mounting medium	Sigma Aldrich	Cat #03989
Putrescine dihyrochloride	Sigma Aldrich	Cat #P5780-5G
DMEM High W/Glutamax	Life Technologies	Cat #61955059
Fetal Bovin Serum	Life Technologies	Cat #10270106
Penicillin-Streptomycin	EuroClone	Cat #ECB3001D
FrameSlides PPS-Membrane 4.0 mm	Leica	Cat #11600294
SuperFrost® Plus adhesive microscope slides	Thermo Fisher Scientific	Cat # 9161155
RNA*later*™ Stabilization Solution	Invitrogen- Thermo Fisher Scientific	Cat #AM7020
Arcturus™ Paradise™ Plus staining components	Applied Biosystems™- Thermo Fisher Scientific	Cat #KIT0312S
Critical commercial assays		
KAPA SYBR FAST qPCR Master Mix (2X)	KAPA Biosystems	Cat #KK4600
2x Fast Q-PCR Master Mix (SYBR, ROX)	SMOBIO	Cat # TQ1211
RNeasy mini-kits	Qiagen	Cat # 74106
PrimeScriptTM RT Reagent Kit with gDNA Eraser (Perfect Real Time)	Takara	Cat # RR047A
Deposited data		
Healthy and Denervated Spatial Transcriptomic Dataset	This paper	GEO: GSE198596
WT snRNAseq Dataset	Chemello et al.[4]	GEO: GSE156498
WT TA 5 Months snRNAseq Dataset	Petrany et al.[16]	GEO: GSM4418992
Preprocessed scMuscle compendium	McKellar et al.[40]	Dryad: https://doi.org/10.5061/dryad.t4b8gtj34
WT and Denervated Gastrocnemius	Lin et al.[10]	GEO: GSE183802
Original code to reproduce analysis and figures	This paper	Zenodo: https://doi.org/10.5281/zenodo.7351244
Experimental models: Cell lines		
C2.C12	ATCC	Cat# CRL-1772
Experimental models: Organisms/strains		
Mouse Model: C57BL/6J	https://www.jax.org/strain/000664	#000664
c179-GAL4: w[*]; P{w[+mW.hs] = GawB}c179 (Fly Stock)	BDSC	Stock #6450
Paox/SmoxRNAi (Official Symbol: CG10561) (Fly Stock)	VDRC	Stock # GD28176
Oligonucleotides		
Primer: Gapdh FW: CACCATCTTCCAGGAGCGAG	This paper	N/A
Primer: Gapdh RV: CCTTCTCCATGGTGGTGAAGAC	This paper	N/A

(Continued on next page)

Continued

REAGENT or RESOURCE	SOURCE	IDENTIFIER
Primer: Amd 1 / 2 FW TGCAATTTTCCCAAATGGAGCA	This paper	N/A
Primer: Amd 1 / 2 RV CTGCTGGGTCAAGCTCACTC	This paper	N/A
Primer: Amd 2 FW: GCTTTCGTCCCCATTAGATGC	This paper	N/A
Primer: Amd 2 RV: CCCTAGAAAGTGGAGGTAACTG	This paper	N/A
Primer: Odc1 FW GCTGTGTCATGGAGAGACCC	This paper	N/A
Primer: Odc1 RV CTCTCCTCTGTGCGG	This paper	N/A
Primer: Smox FW AGCTCCAAGACAGCGCATAG	This paper	N/A
Primer: Smox RV GGTCCAGGGATTGTTCTGGG	This paper	N/A
Primer: Trim63 FW AACTTGTGGAGACCGCCATC	This paper	N/A
Primer: Trim63 RV TGGAGGCTTCTACAATGCTCTT	This paper	N/A
Primer: Fbxo32 FW CTCAGAGAGGCAGATTCGCA	This paper	N/A
Primer: Fbxo32 RV GGTGACCCCATACTGCTCTC	This paper	N/A
Software and algorithms		
GraphPad Prism 8		http://www.graphpad.com
ImageJ	Schneider et al.[50]	https://imagej.nih.gov/ij/
Space Ranger 1.1.0	10X Genomics	https://support.10xgenomics.com/spatial-gene-expression/software/pipelines/1.1/what-is-space-ranger
Seurat 4.1.0	Hao and Hao et al.[41]	https://github.com/satijalab/seurat
dplyr 1.0.7	Wickham H et al.[51]	https://CRAN.R-project.org/package=dplyr
cowplot_1.1.1	Wilke et al.[52]	https://cloud.r-project.org/package=cowplot
ggplot2 3.3.5	Wickham et al.[53]	https://ggplot2.tidyverse.org
Sctransform 0.3.3	Hafemeister & Satija[54]	https://cran.r-project.org/web/packages/sctransform/index.html
Patchwork 1.1.1	Pedersen[55]	https://cran.r-project.org/web/packages/patchwork/index.html
Viridis 0.6.1	Garnier et al.[56]	https://sjmgarnier.github.io/viridis/
gprofiler2 0.2.1	Peterson et al.[57]	https://biit.cs.ut.ee/gprofiler/page/r
DoubletFinder_2.0.3	McGinnis et al.[58]	https://github.com/chris-mcginnis-ucsf/DoubletFinder/
EBImage_4.36.0	Pau et al.[59]	https://bioconductor.org/packages/release/bioc/html/EBImage.html
QuantStudio 7 Flex	Appliedbiosystems, Thermo Scientific	N/A
NanoDrop ONE[c] spectrophotometer	Thermo Scientific	ND-ONE-W
LSM 900 with Airyscan2	Zeiss	N/A

RESOURCE AVAILABILITY

Lead contact
Further information and requests for resources and reagents should be directed to and will be fulfilled by the lead contact, Madaro Luca (luca.madaro@uniroma1.it).

Materials availability
The reagent and material for this study will be available on reasonable request.

Data and code availability
- All the data reported in this paper will be shared by the lead contact upon request. Raw data for healthy and denervated muscle have been deposited at GEO and are publicly available as of the date of publication. The accession number is listed in the key resource table (GEO: GSE198596). The Spatial Transcriptomics Dataset can be freely inspected on SpatialMuscle interactive Platform (https://spatialmuscle.shinyapps.io/spatialmuscle/).
- This paper re-analyzes existing, publicly available data. Accession numbers for these datasets are listed in the key resource table.
- All original code has been deposited on Zenodo and is publicly available as of the date of publication. DOIs are listed in the key resources table (Zenodo: https://doi.org/10.5281/zenodo.7351244).
- Any additional information required to reanalyze the data reported in this paper is available from the lead contact upon request.

EXPERIMENTAL MODEL AND SUBJECT DETAILS

Mouse lines
Mouse line used in this study was:

   C57BL/6J were provided by the Jackson Laboratory (Bar Harbor, USA).

   All mice were maintained in a pathogen-free animal facility under standard 12h light/12h dark cycle at 21°C with access to red house and to standard chow and water ad libitum. Three-month-old male mice were used for ex-vivo experiments. All experiments in this study were performed in accordance with protocols approved by Italian Ministry of Health and University of Rome 1 "Sapienza" (Rome). The study is compliant with all relevant ethical regulations regarding animal research and in the respect of the principles of the 3Rs (Replacement, Reduction and Refinement).

METHOD DETAILS

Denervation
Unilateral hindlimb denervation was performed by clamping the right sciatic nerve under anesthesia via intraperitoneal injection of 40 mg/kg ketamine (Zoletil®) and 10 mg/kg xylazine (Rampum). After the exposure of sciatic nerve, cutting the skin near the knee, the nerve was crushed with chirurgical tweezer three times for 10 sec each time. The lesion was sutured with 3M Vetbond Tissue Adhesive after the operation. After surgery, the mice were monitored until the sacrifice date. After the operation the animals were monitored, and the actual denervation assessed by a grip test.

Spatial RNA sequencing library preparation
TA muscles were isolated, embedded in OCT (VWR), and flash frozen in liquid nitrogen for 15 s, after those muscles were stored at temperature of −80 until the cryosection. Spatially tagged cDNA libraries were built using a Visium Spatial Gene Expression 3′ Library Construction v1 Kit (10x Genomics, PN-1000187; Pleasanton, CA). The optimal tissue permeabilization time for 10 μm-thick sections was found to be 15 min using a 10x Genomics Visium Tissue Optimization Kit (PN-1000193). Immunofluorescence-stained tissue sections were imaged using a Zeiss confocal microscope (LSM 900 with Airyscan2) with a mechanical plate, and the images were then edited using ImageJ® software.

   The primary probes used for immunofluorescence were rabbit anti-laminin (1:200), mouse anti-collagen-1 (1:200), and BTX 488 (1:200). Antibody binding specificity was revealed using secondary antibodies coupled to Alexa Fluor 594 or 647. Libraries were generated from cDNA following the manufacturer's instructions and checked with both a Qubit 2.0 Fluorometer (Invitrogen, Carlsbad, CA) and an Agilent Bioanalyzer DNA assay (Agilent Technologies, Santa Clara, CA). Libraries were then sequenced in paired-end 150 bp mode on a NovaSeq 6000 system (Illumina, San Diego, CA). The frames around the capture area on the Visium slide were aligned manually, and spots distributed across the tissue were selected using Loop Browser v5.0.0 software (10x Genomics). The sequencing data were then aligned to the mouse reference genome (mm10) using the Space Ranger v1.0.0 pipeline (10x Genomics) to generate a feature-by-spot-barcode expression matrix. Analysis was performed using Seurat v4 (the R workflow can be assessed and reproduced in R Markdown - see data and code availability). Briefly, each section was loaded using the Load10X_Spatial () function and preprocessed separately by applying sctransform normalization. After this initial step, sections were integrated using IntegrateData () with the normalization method parameter set to "SCT"

and using all features from the different datasets as features for integration. Integrated dataset was normalized using SCT. After clustering and cell population identification, the most highly differentially expressed genes were identified using the ''FindAllMarkers'' function with the following parameters: only.pos = TRUE, min.pct = 0.25, and logfc.threshold = 0.25. Cell type prediction scores were inferred using the publicly available snRNA-seq WT dataset from Chemello et al. as a reference [4]. Anchors between the two datasets were identified using FindTransferAnchor with the following parameters (normalization.method = ''SCT'', = and reduction = "cca"), and label transfer was performed with the default parameters. GO enrichment analysis was performed with gprofiler2 using as input cluster markers present at least in 50% of each cluster (pct.1 > 0.5). Average expression data were obtained using "AverageExrepssion" functions and subsequently filtered for expression above 0.1 and lg2FC (3days vs CTR) >-0.3 or <0.3. KEGG pathway analysis of genes upregulated in 3days vs CTR was performed using Enrichr.[60] After analysis, for visualization purposes, images were reoriented to display the EDL at the bottom-left corner. When displaying gene expression for the whole dataset across the different images, maximum value for scale limit was set to 99th percentile of total expression across samples to harmonize scales and improve visualization. The 5 months WT dataset from Petrany et al.[16] used to generate the dotplot in Figure S5 has been obtained by subsetting the fully processed scMuscle compendium seurat object from McKellar et al.[40] available for download on Dryad (https://doi.org/10.5061/dryad.t4b8gtj34).

Laser microdissection

TA muscles were isolated, embedded in OCT, flash frozen in liquid nitrogen and stored at −80°C. Ten-millimeter frozen sections cut on a cryostat (Leica CM1850) were mounted on PET-membrane 1.4 mm frame slides (Leica) previously cleaned with RNase Away (Molecular Bio Products) and UV treated for 45 min under a sterile hood. NADH-TR stained muscle (protocol of staining described below) was performed to visualize the tissue structure. The glycolytic and oxidative portions of the TA muscles of 5 mice in the CTR group and 5 mice in the crush-3 and -30 days group were microdissected with a laser microdissection system (Leica LMD6) and recovered in RNAlater reagent (QIAGEN).

RNA analysis by quantitative PCR

Total RNA was extracted from total muscle or dissected specimens (look above) using Qiagen RNeasy mini kits following the manufacturer's protocol. Total RNA was quantified with a NanoDrop ONE^c spectrophotometer (Thermo Scientific). First-strand cDNA was synthesized from the total RNA using a PrimeScript^{TM} RT Reagent Kit with gDNA Eraser (Takara) following the manufacturer's protocols. The generated cDNA was used as a template in real-time PCR with Fast Q-PCR Master Mix (SMOBIO), which was run on a QuantStudio 7 Flex (Applied Biosystems, Thermo Scientific) machine with three-step amplification (1. template denature and enzyme activation step 95°C 2 min for 1 cycle – 2. denature step 95°C 15 sec and 3. annealing/extension steps 60°C 60 sec, 2 and 3 steps for 40 cycles) and melting curve analysis. Each reaction in the quantitative real-time PCR consisted of 2x Fast Q-PCR Master Mix (SYBR, ROX), 2.5 mM forward and reverse primers and 10 ng of cDNA. Relative gene expression values were normalized by dividing the specific expression value by the glyceraldehyde 3-phosphate (*Gapdh*) or actin beta (*Actb*) expression value and calculated using the 2$^{-\Delta\Delta CT}$ method.

Histological staining

For the Immunofluorescence staining, 10 μm muscle cryosectios were fixed in 4% PFA (MilliporeSigma, P6148) for 10 minutes or permeabilized with 100% acetone for 1 minute at room temperature. Muscle sections were then blocked for 1 hour with a solution containing 4% BSA (MilliporeSigma, A7030-100G) in PBS. The primary antibodies used for immunofluorescences are mouse anti-synaptophysin (1:300, Invitrogen, PA1-1043); rabbit anti-laminin (1:300, MilliporeSigma, L9393). The primary antibody immunostaining was performed overnight at 4°C, and then the antibody binding specificity was revealed using secondary antibodies coupled to Alexa Fluor 488, 594, or 647. AChRs were revealed with fluorescently labeled BTX (1:300 Alexa 594, Invitrogen, B13423 or Alexa 488, Invitrogen, B13422). Sections were incubated with DAPI (Thermo Fisher Scientific, D1306) in PBS for 5 minutes for nuclear staining, washed in PBS, and mounted with glycerol (3:1 in PBS). The transverse sections were visualized on a Zeiss confocal microscope then edited using the ImageJ software.

For the myosin immunofluorescent staining, 10 μm muscle cryosectios were then blocked with a solution containing 10 % Goat Serum in PBS for 10 min and then with a solution containing 4% BSA (PanReac AppliChem, A1391,0100) in PBS for 30 min. The primary antibodies used for immunofluorescences are mouse anti-myosin heavy chain, Type 2B BF-F3 (1:50 for IF), mouse anti-myosin heavy chain Type 2A 2F7 (1:10 for IF); rabbit anti-laminin (1:200, Sigma-Aldrich, L9393). The primary antibody immunostaining was performed overnight at 4°C, and then the antibody binding specificity was revealed using secondary antibodies coupled to Alexa Fluor 488, 555, or 647. Sections were incubated with DAPI (Thermo Fisher Scientific, D1306) in PBS for 5 minutes for nuclear staining, washed in PBS, and mounted with glycerol (3:1 in PBS). The transverse sections were visualized on a Zeiss confocal microscope.

For Sirius red staining muscle cryosections were fixed for 1 h at 56 °C in Bouin's solution and then stained in a Picro-Sirius red (0.1%) solution for 1 h protected from light. After a brief wash in acidified water (0.5% vol/vol), the sections were fixed in 100% ethanol, and the final dehydration step was performed in 100% toluene. The sections were mounted with EUKITT mounting medium (Sigma–Aldrich) and visualized using a Zeiss Imager.A2.

For H&E staining, the sections were fixed in 4% PFA for 10 min, washed in PBS and then stained in hematoxylin for 12 min and eosin for 30 sec. For NADH staining, the sections were placed in buffer solution (0.1 M Tris HCl, pH 7.5, in ddH$_2$O) for 5 min. Then, they were stained with NADH solution (2 mg of NADH and 4 mg of NBT in 0.1 M Tris HCl, pH 7.5, in ddH$_2$O) for 1 h at 37°

in the dark. After removing the dye, all muscle sections were further dried in gradually increasing concentrations of ethanol in water, and after fixation in 100% toluene, they were mounted with EUKITT mounting medium (Sigma–Aldrich). The sections were imaged using a Zeiss Imager A2.

C2.C12 culture

C2.12 (C2C12) myogenic cells were obtained from ATCC and cultured on 24-well plates in growth medium (DMEM [-Pyruvate], Gibco, 61965–026; supplemented with 10% of FBS and 1% of penicillin/ streptomycin). Myogenic differentiation was induced by shifting the cells in differentiation medium (DMEM [-Pyruvate] complemented with 1% penicillin/streptomycin and 2% horse serum). C2C12 myotubes were treated with putrescine dihydrochloride (P5780- Sigma–Aldrich) 2 mM for 48 hours in differentiation medium.

To analyze the morphology of myotubes, these were fixed in 4% PFA for 10 min at RT (MilliporeSigma, P6148) for 10 minutes and permeabilized with 0.1% Triton X-100 for 10 minutes at RT. Cultured cells were then blocked for 1 hour with a solution containing 4% BSA (MilliporeSigma, A7030-100G) in PBS. The primary antibody (mouse anti-myosin; 1:20, DSHB, MF20) immunostaining was performed overnight at 4°C, and then the antibody binding specificity was revealed using secondary antibodies coupled to Alexa Fluor 488 (goat anti-mouse Alexa Fluor 488 [1:300, A32731). Sections were washed in PBS and mounted with glycerol (3:1 in PBS).

Myotubes were visualized on a Zeiss confocal microscope. Then the morphological analysis of diameters was measured with ImageJ software. The figures reported are representative of all the examined fields.

Drosophila strains and rearing conditions

Drosophila stocks were maintained on standard fly food (25 g/L corn flour, 5 g/L lyophilized agar, 50 g/L sugar, 50 g/L fresh yeast, 2,5 mL/L Tegosept [10% in ethanol], and 2,5 mL/L propionic acid). All experiments were performed in the same conditions, at 29°C in a 12 hr light/dark cycle. The c179-GAL4 driver (BDSC # 6450) and the RNAi line (VDRC #GD28176) used have been previously described and available from the Bloomington stock center (https://bdsc.indiana.edu/) or Vienna Drosophila resource center (https://stockcenter.vdrc.at/control/main) respectively.

Climbing assays

The locomotion activity was measured by testing the Drosophila natural drive for negative geotaxis. Freshly enclosed flies were transferred in new food vials and aged for 3, 7 or 10 days. A female-male ratio of 1:1 was maintained. After this period, they were moved, without anesthesia, to 50 mL falcon tube, tapped to the bottom and let climb up. The number of flies that reached the top of the tube in 10 s was counted and converted in percentage.

Polyamine analysis

Polyamine content was determined by gas chromatography-mass spectrometry (GC-MS) and the values were normalized by muscle weight. TA muscles pulverized in liquid nitrogen were resuspended in 0.2 M $HClO_4$ and homogenized in an ice-bath using an ultra-turrax T8 blender. The homogenized tissue was centrifuged at 13,000× g for 15 min at 4°C; 0.5 mL of supernatant was spiked with internal standard 1,6-diaminohexane and adjusted to pH $\geq$ 12 with 0.5 mL of 5 M NaOH. The samples were then subjected to sequential N-ethoxycarbonylation and N-pentafluoropropionylation. For DM2 samples, biopsies were also resuspended in 0.2 M $HClO_4$ and processed as described above. GC-MS analyses were performed with an Agilent 7890B gas chromatograph coupled to a 5977B quadrupole mass selective detector (Agilent Technologies, Palo Alto, CA). Chromatographic separations were carried out with an Agilent HP-5ms fused-silica capillary column. Mass spectrometric analysis was performed simultaneously in TIC (mass range scan from m/z 50 to 800 at a rate of 0.42 scans s–1) and SIM mode (put, m/z 405; spd, m/z 580, N1-acetyl-spm, m/z 637; spm, m/z 709).

Western Blot

Protein extracts were derived from 5 muscle carcasses of third instar larvae, lysed in sample buffer, fractionated by SDS-PAGE and transferred to nitrocellulose membrane. Primary antibodies anti-Smox rabbit (1:250; FabGennix SMOX-101AP); anti-Vibrator goat (alias Giotto; 1:5000).[49] As secondary antibody we used an anti-rabbit HRP-conjugated antibody (GE Healthcare) diluted 1:5000 in TBS-Tween 0.1% (GE Healthcare). Detection was performed by using Western Bright ECL (BioRad). Unprocessed blot was shown in Figure S5F.

Figure design

The graphical abstract, Figures 1A, 7E and S5A were created with BioRender (https://biorender.com/), license to Dr. Madaro Luca.

QUANTIFICATION AND STATISTICAL ANALYSIS

Statistical analysis

Data are presented as the mean ± SEM. Comparisons were conducted using Student's t test, assuming a two-tailed distribution, or by one-way ANOVA with Tukey's post test, with significance defined as $p < 0.05$ (*), $p < 0.01$ (**), or $p < 0.001$ (***). The number of biological replicates for each experiment is indicated in the corresponding figure legend. Histological and immunofluorescence images are representative of at least 3 different experiments/animals.